State Quadrant Modeling Approach: Simplifying High-Precision Modeling of DC-DC Converters for Model-Based Control Strategies

Ruiheng Guo, Wentao Huang, *Senior Member, IEEE*, Moduo Yu, *Member, IEEE*, Canbing Li, *Senior Member, IEEE*, Yuyang Zhang, Hongbiao Li, and Zhushun Cao, *Graduate Student Member, IEEE*

***Abstract*—DC–DC converters switch from continuous conduction mode (CCM) to discontinuous conduction mode when the inductor current drops to zero in scenarios, such as load reduction and load pulse. CCM model-based control methods suffer from degraded performance under such conditions, whereas hybrid model-based control methods are limited by complex mathematical formulations of logical variables, piecewise structures, and inequalities and high computational costs. This article proposes a state quadrant modeling approach, which includes circuit state classification and state descriptor construction, offering high-precision and simplifying models for model-based control. The circuit state classification method identifies circuit states based on freewheeling conditions and current trends, ensuring comprehensive coverage of operating scenarios and enhancing modeling accuracy. Furthermore, the state descriptor construction method employs logical operations to derive one or two logical variables that uniformly represent different circuit states, eliminating the need for inequalities and piecewise structures. This method is highly scalable and applicable to single-inductor, dual-inductor, multiphase, and isolated converters. It significantly enhances control performance, simplifies design, and improves computational efficiency when integrated into model-based control methods. Case studies demonstrate that the proposed models achieve 99.99% accuracy relative to simulink results and 98.99% accuracy relative to experimental results. They also reduce computation time by 36.85% in model predictive control and decrease voltage response time by 35.69%.**

***Index Terms*—Continuous conduction mode (CCM), dc–dc converter, discontinuous conduction mode (DCM), model-based control, state quadrant modeling.**

I. Introduction

In recent years, the rapid advancement of dc microgrid and transportation electrification technologies has significantly elevated the importance of both dc power distribution and conversion [1]. As a cornerstone of these technologies, dc–dc converters play a pivotal role across various applications, including electric vehicles [2], electric ships [3], and renewable energy systems [4]. Mathematical models form the theoretical foundation for controller design, stability analysis, and performance optimization [5], [6]. With the growing deployment of dc–dc converters in complex and mission-critical scenarios, greater emphasis has been placed on improving their transient performance [7], thus driving the need for accurate and adaptable models to support advanced control methods.

High-power dc–dc converters predominantly operate in continuous conduction mode (CCM), and thus most controller designs are based on CCM models [8]. However, under certain operating conditions, such as load variations, the inductor current becomes discontinuous, causing the converter to switch between CCM and discontinuous conduction mode (DCM) [9]. In such cases, CCM models fail to capture converter dynamics, resulting in degraded controller performance or even instability [10], [11]. Consequently, there is a pressing need for models that not only accurately describe converter behavior in different modes but also seamlessly integrate with existing model-based control frameworks.

Various models have been proposed, concentrating on averaging methods [12], such as state-space averaging, averaged switch modeling [13], and improved averaging methods [14]. The state-space average model, derived from the switch model, weights state variables based on the switch's ON and OFF times within a cycle. Average models, with their clear physical interpretation and analytical expressions, have become the mainstream for researching dc–dc converter control methods [15]. However, their applicability is limited to CCM. When current becomes discontinuous, these models struggle to maintain accuracy [16], leading to significant errors and even failure to predict transient trend of current and voltage.

DCM models have been developed to account for discontinuous current scenarios. Qiu et al. [17] presented a small-signal model for dc–dc converters in DCM, capturing the nonlinear current effects of parasitic resistances. Tofoli [18] introduced a DCM modeling approach for dc–dc converters using the four-state switching cell. Kim et al. [19] provided a thorough analysis of a two-phase interleaved buck converter in DCM,

Received 29 May 2025; revised 29 July 2025; accepted 25 August 2025. Date of publication 4 September 2025; date of current version 23 December 2025. Recommended for publication by Associate Editor D. O Neacsu. *(Corresponding author: Wentao Huang.)*

Ruiheng Guo, Wentao Huang, Moduo Yu, Canbing Li, and Zhushun Cao are with the Department of Electrical Engineering, Shanghai Jiao Tong University, Shanghai 200240, China (e-mail: hwt8989@sjtu.edu.cn).

Yuyang Zhang is with China Power Complete Equipment Company, Ltd., Beijing 100120, China.

Hongbiao Li is with Shanghai KeLiang Information Technology Company, Ltd., Shanghai 201103, China.

This article has supplementary material provided by the authors and color versions of one or more figures available at https://doi.org/10.1109/TPEL.2025.3605343.

Digital Object Identifier 10.1109/TPEL.2025.3605343

and establishes a model that accounts for inductive coupling. While these models effectively complement CCM models by describing converter behavior during DCM, their applicability is limited to this single mode.

Existing model-based control methods for dc–dc converters are mainly developed using single-mode models to improve performance under complex scenarios. For example, the damping ratio control proposed in [20] provides a parameter-free solution for ship pulse loads, addressing issues with fixed control parameters in extreme power step scenarios. The adaptive voltage-guaranteed control in [21] improves the voltage stability of buck converters when dealing with constant power loads that exhibit negative incremental impedance. The model predictive control in [22] reduces voltage fluctuations in energy storage systems with frequent power variations. The composite finite-time controller in [23] enhances the power sharing and stabilization of fuel cell-supercapacitor systems in electric aircraft. These examples underscore the critical importance of high-performance control for dc–dc converters across diverse applications. However, single-mode models are incapable of capturing the transitions between CCM and DCM, thereby leading to diminished controller performance.

Hybrid modeling methods have been developed to provide a unified description of both CCM and DCM, covering various paradigms [24], [25]. The authors in [26] and [27] proposed a hybrid small-signal model integrating CCM and DCM, but its accuracy drops under large disturbances. Data-driven modeling has also been used, with Kumar and Agarwal [28], developing a supervised learning-based hybrid model for a boost converter, and Li et al. [29], creating a physics-informed neural network-based hybrid model for a full-bridge converter. However, neural networks suffer from an uninterpretable structure, precluding their direct use in controller development. Logic-driven modeling techniques are currently the most promising hybrid modeling approaches, as they avoid linearization approximations and offer transparency. Beg et al. [30] proposed a hybrid automaton model with logic-based switching for different circuit states, and Hejri [31] introduced the mixed logical dynamic (MLD) method to simplify descriptions of continuous and discrete variables. However, MLD-based modeling still introduces many constraints and logical variables, complicating the model. Simplifying MLD is an important area of improvement. Han [32] introduced a biswitching status modeling (BSM) method that reduces logical variables and constraints and provides a unified framework for hybrid modeling of buck, boost, and buck–boost converters. Fang [33] introduced a multimode sequence modeling approach that addresses the shortcomings of BSM in high-frequency converters, including mode skipping and the inability to incorporate parasitic parameters, and further simplifies constraints and logical variables. Logic-driven hybrid modeling methods have been effective in capturing the transient behavior of dc–dc converters. However, these methods have some limitations: 1) They often depend on piecewise structures and inequality constraints, which are generally unfavorable in controller design and notably increase complexity and analytical difficulty compared to the conventional form $\dot{\boldsymbol{x}} = f(\boldsymbol{x}, \boldsymbol{u})$. 2) The structural differences between the hybrid models and CCM models hinder seamless integration into existing CCM model-based control frameworks. This mismatch may lead to underutilization of prior research. 3) These methods focus primarily on specific dc–dc converters, such as buck and boost converters, which are simple single-inductor topologies. Their applicability to other types of converters, such as dual-inductor, multiphase, and isolated topologies, remains unclear.

To address the aforementioned gaps, this article proposes a state quadrant modeling approach. First, it comprehensively classifies the circuit states based on the inductor's freewheeling conditions and the trend of inductor current, ensuring that all circuit states are accounted. Second, it utilizes logical operations to derive state descriptors, enabling a comprehensive representation of various circuit states with 1 and 2 descriptors. The proposed approach has the following advantages:

1) *High precision:* The proposed models provide a unified description of the system behavior under both in CCM and DCM, achieving an accuracy rate of 99.99%. This establishes a solid foundation for enhancing the performance of model-based controllers.
2) *Simplification:* The proposed models introduce only 1 and 2 additional logical variables without the need for inequalities or piecewise structures. Consequently, they can be seamlessly integrated into existing control methods based on CCM models.
3) *Versatility:* The presented approach features a standardized modeling process and excellent scalability, making it applicable to various converters, including single-inductor, dual-inductor, multiphase, isolated, and bidirectional converters.

The rest of this article is organized as follows. Section II describes model failure scenarios. Section III details the state quadrant modeling approach. Section IV discusses the numerical solution methods of the proposed models. Section V details the application of the proposed models in a model-based control method. Section VI presents case studies to illustrate the effectiveness of the proposed model. Finally, Section VII concludes this article.

II. Model Failure Analysis

This section centers on the analysis of model failure using the CCM model of buck converters as an example. The CCM model is presented in the following equation:

$$\begin{bmatrix} L\frac{di_{\mathrm{L}}}{dt} \\ C\frac{du_{\mathrm{C}}}{dt} \end{bmatrix} = \begin{bmatrix} E-u_{\mathrm{c}} & -u_{\mathrm{C}} \\ i_{\mathrm{L}}-\frac{u_{\mathrm{C}}}{R} & i_{\mathrm{L}}-\frac{u_{\mathrm{C}}}{R} \end{bmatrix} \begin{bmatrix} u \\ 1-u \end{bmatrix} \tag{1}$$

where u is the control variable, which can be either a switch signal $g \in \{0, 1\}$ or a duty cycle $d \in [0, 1]$.

Significant errors can arise from (1) when the inductor current becomes discontinuous, as the model is based on the assumption that the inductor current remains continuous and does not drop to zero. For instance, under external disturbances, when the inductor current falls to zero, the i_{L} derived from the solution of (1) (with $u = 0$) may become negative, as depicted in (2). The

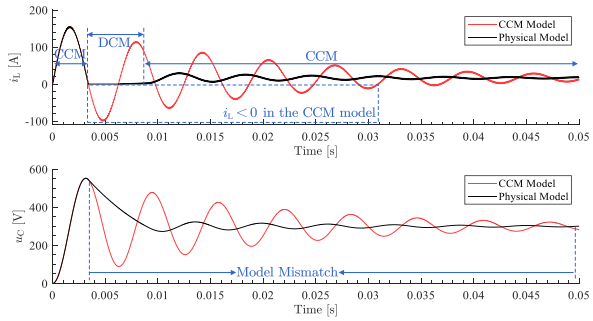

Fig. 1. Model failure scenario 1: Startup with light load.

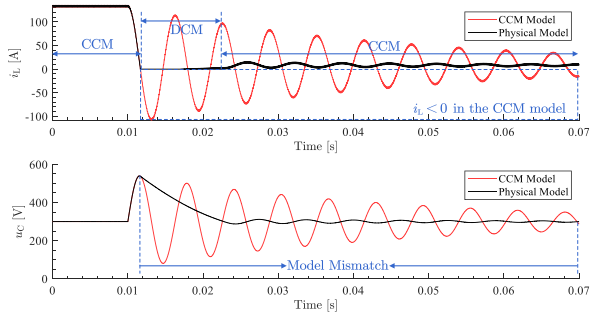

Fig. 2. Model failure scenario 2: Load disturbance.

result contradicts the actual physical behavior.

$$i_{\mathrm{L}} = -\frac{CRu_{\mathrm{C}}(0)\mathrm{e}^{-\frac{t\sqrt{L^2-4CLR^2}}{2CLR}}\mathrm{e}^{-\frac{t}{2CR}}\left(\mathrm{e}^{\frac{t\sqrt{L^2-4CLR^2}}{CLR}}-1\right)}{\sqrt{L^2-4CLR^2}} < 0 \tag{2}$$

where $u_{\mathrm{C}}(0)$ is the initial voltage of the capacitor.

To further elucidate the discrepancies between the physical model and the CCM model represented by (1), we conducted tests on a buck converter under typical operating scenarios. The specifications of the converter are as follows: an input voltage of 400 V, a rated output voltage of 300 V, an inductance of 2 mH, and a capacitance of 0.5 mF.

Scenario 1—Startup with light loads: Consider a system with an initial load of 5 kW, which employs a fixed duty cycle control method. Fig. 1 illustrates a critical phenomenon observed during the startup process: around 3 ms, the calculated inductor current turns negative. This anomaly not only contradicts physical principles but also initiates a cascade of subsequent calculation errors.

Scenario 2—Load disturbances: The system had reached a steady state under a 40 kW load when, at 10 ms, a 37.5 kW load was removed. The control method continued to use a fixed duty cycle. Fig. 2 shows that following the load disturbance, the CCM model encountered a calculation error at 2 ms. This error led to significant discrepancies between the computed values of the capacitor voltage and inductor current and their actual values. These results highlight the CCM model's inability to accurately predict system behavior during dynamic load changes.

Scenario 3—Pulse loads: The converter is tasked with supplying power to a pulse load characterized by specific parameters:

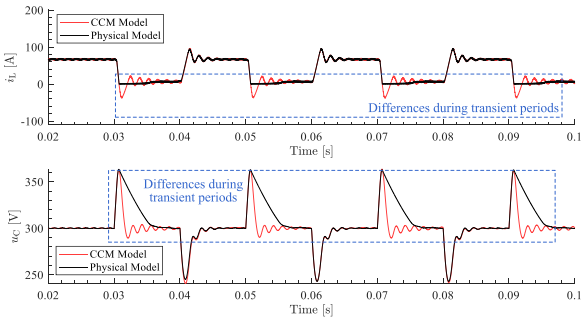

Fig. 3. Model failure scenario 3: Pulse load.

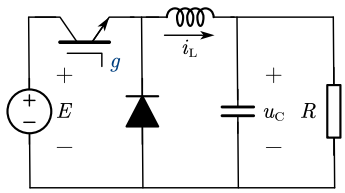

Fig. 4. Topology of buck converters.

$P = 20\,\mathrm{kW}$, $D = 50\%$, and $T = 20\mathrm{ms}$. The control method employs model prediction control (MPC), which is based on (1). Fig. 3 demonstrates that the CCM model's depiction of the system's transient behavior significantly deviates from the actual behavior. The result indicates that the divergence between the CCM model and the physical system could pose a significant challenge to the effectiveness of model-based control methods.

Based on the above analysis, the mismatch between the CCM model and the physical model not only limits the in-depth study of the transient processes in high-power dc–dc converters but also hinders the effective application of advanced control methods. Hybrid models provide viable solutions for model-based control, but their inclusion of logical variables, piecewise structures, and inequalities makes them difficult to apply. This study aims to develop high-precision and simplifying models of dc–dc converters, to facilitate the development of high-performance model-based controllers.

III. State Quadrant Modeling Approach for DC–DC Converters

This section first details the state quadrant modeling method using a buck converter and a cuk converter as examples. It then summarizes and establishes a standard modeling procedure, and finally applies it to various types of dc–dc converters, obtaining models for typical dc–dc converters.

A. State Quadrant Modeling: Buck Converter

The topology of buck converters is shown in Fig. 4. First, we derive the state-space equations for the case when $g = 1$. When the inductor is freewheeling, the switch is conducting; conversely, when the inductor is not freewheeling, whether the switch conducts depend on the trend of the inductor current. Specifically, if the inductor current exhibits an increasing trend, it will not trigger the reverse cutoff of the switch; conversely, if

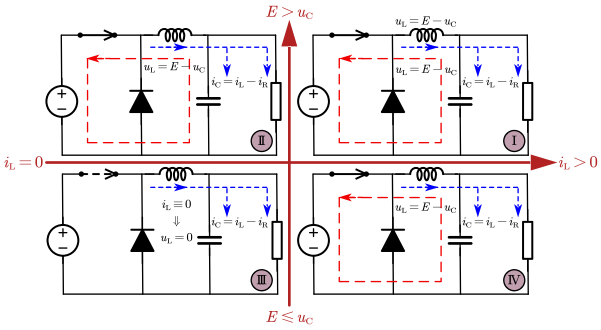

Fig. 5. State quadrant analysis of the buck converter ($g = 1$).

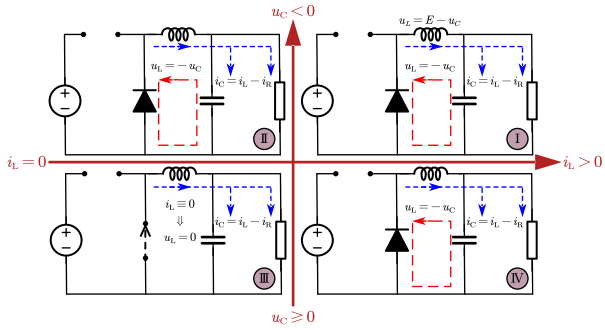

Fig. 6. State quadrant analysis of the buck converter ($g = 0$).

the inductor current exhibits a decreasing trend, it will induce the switch to cut off. Therefore, the circuit state is determined by whether the inductor is freewheeling and the trend of the inductor current.

The freewheeling of the inductor depends on whether i_{L} is zero. The trend of the inductor current depends on the voltage difference across the inductor when the switch is assumed to be conducted. When this voltage difference is positive, the trend is positive; otherwise, it is negative. We classify the circuit states based on whether $i_{\mathrm{L}} > 0$ and the voltage difference across the inductor, as shown in Fig. 5. In this article, a state quadrant is defined as the operating region determined by the inductor conduction state and the current trend. The figure includes four quadrants, where the horizontal axis represents the inductor's freewheeling status, and the vertical axis represents the trend of the inductor current.

In any quadrant, the inductor, capacitor, and load are connected at a common node without any additional power electronic components influencing them. Consequently, the current relationship $C\frac{du_{\mathrm{C}}}{dt} = i_{\mathrm{L}} - \frac{u_{\mathrm{C}}}{R}$ always holds. Next, we focus on the differential equation of the inductor current.

1) *Quadrant I* $\Leftrightarrow i_{\mathrm{L}} > 0$ *and* $E > u_{\mathrm{C}}$*:* Due to $i_{\mathrm{L}} > 0$, the inductor's freewheeling function causes the switch to conduct. Therefore, the inductor voltage $L\frac{di_{\mathrm{L}}}{dt}$ is $E - u_{\mathrm{C}}$.
2) *Quadrant II* $\Leftrightarrow i_{\mathrm{L}} = 0$ *and* $E > u_{\mathrm{C}}$*:* The voltage difference $E - u_{\mathrm{C}}$ causes the rate of change of inductor current to be positive, indicating an increasing trend in inductor current. Therefore, this situation does not trigger the reverse cutoff of the switch, so $L\frac{di_{\mathrm{L}}}{dt} = E - u_{\mathrm{C}}$.
3) *Quadrant III* $\Leftrightarrow i_{\mathrm{L}} = 0$ *and* $E \leqslant u_{\mathrm{C}}$*:* The voltage difference $E - u_{\mathrm{C}} \leqslant 0$ results in a negative rate of change for the inductor current, which means that the inductor current is decreasing. This situation will trigger the reverse cutoff of the switch, maintaining the current at 0. Therefore, the inductor voltage $L\frac{di_{\mathrm{L}}}{dt}$ is 0.
4) *Quadrant IV* $\Leftrightarrow i_{\mathrm{L}} > 0$ *and* $E \leqslant u_{\mathrm{C}}$*:* The switch remains conductive because $i_{\mathrm{L}} > 0$, allowing the inductor to perform its freewheeling function. In this case, the inductor voltage $L\frac{di_{\mathrm{L}}}{dt}$ is $E - u_{\mathrm{C}}$.

The structured analysis of the above quadrants is summarized in (3). The first and second columns represent the circuit states, while the third column shows the inductor voltage under these states. This formula illustrates the variations in the inductor voltage under different states.

$$\begin{array}{cc|cc} \text{Freewheeling} & \text{Trend} & L\frac{di_{\mathrm{L}}}{dt} & C\frac{du_{\mathrm{C}}}{dt} \\ i_{\mathrm{L}} > 0 & E - u_{\mathrm{C}} > 0 & E - u_{\mathrm{C}} & i_{\mathrm{L}} - \frac{u_{\mathrm{C}}}{R} \\ i_{\mathrm{L}} > 0 & E - u_{\mathrm{C}} \leqslant 0 & E - u_{\mathrm{C}} & i_{\mathrm{L}} - \frac{u_{\mathrm{C}}}{R} \\ i_{\mathrm{L}} = 0 & E - u_{\mathrm{C}} > 0 & E - u_{\mathrm{C}} & i_{\mathrm{L}} - \frac{u_{\mathrm{C}}}{R} \\ i_{\mathrm{L}} = 0 & E - u_{\mathrm{C}} \leqslant 0 & 0 & i_{\mathrm{L}} - \frac{u_{\mathrm{C}}}{R}. \end{array} \tag{3}$$

The unified expressions for $L\frac{di_{\mathrm{L}}}{dt}$ can be represented as the sum of products of logical expressions and differential equations, as shown in the following:

$$\begin{aligned} L\frac{di_{\mathrm{L}}}{dt} = {} & [(i_{\mathrm{L}} > 0) \wedge (E > u_{\mathrm{C}})] \cdot (E - u_{\mathrm{C}}) \\ & + [(i_{\mathrm{L}} > 0) \wedge (E \leqslant u_{\mathrm{C}})] \cdot (E - u_{\mathrm{C}}) \\ & + [(i_{\mathrm{L}} = 0) \wedge (E > u_{\mathrm{C}})] \cdot (E - u_{\mathrm{C}}) \\ & + [(i_{\mathrm{L}} = 0) \wedge (E \leqslant u_{\mathrm{C}})] \cdot 0 \\ = {} & \{[(i_{\mathrm{L}} > 0) \wedge (E \leqslant u_{\mathrm{C}})] \vee [(i_{\mathrm{L}} = 0) \wedge (E > u_{\mathrm{C}})] \vee \\ & [(i_{\mathrm{L}} = 0) \wedge (E > u_{\mathrm{C}})]\} \cdot (E - u_{\mathrm{C}}) \end{aligned} \tag{4}$$

where $\vee$ and $\wedge$ represent the logical OR and AND operations.

From (3), $L\frac{di_{\mathrm{L}}}{dt}$ can be expressed as $\eta_1(E - u_{\mathrm{C}})$, where η_1 are logical variables taking values of 0 or 1. Given that η_1 encapsulates the circuit's status, we refer to it as the state descriptor. These state descriptors can be further simplified, as shown in the following:

$$\begin{aligned} \eta_1 = {} & [(i_{\mathrm{L}} > 0) \wedge (E > u_{\mathrm{C}})] \vee [(i_{\mathrm{L}} > 0) \wedge (E \leqslant u_{\mathrm{C}})] \\ & \vee [(i_{\mathrm{L}} = 0) \wedge (E > u_{\mathrm{C}})] \\ = {} & (i_{\mathrm{L}} > 0) \vee [(i_{\mathrm{L}} = 0) \wedge (E > u_{\mathrm{C}})] \\ = {} & (i_{\mathrm{L}} > 0) \vee (E > u_{\mathrm{C}}). \end{aligned} \tag{5}$$

Similarly, using the state quadrant method, we can deduce the logical relationship between various circuit states and inductor voltage when $g = 0$. The state quadrant diagram is shown in Fig. 6, and the mapping of circuit states to inductor voltage and

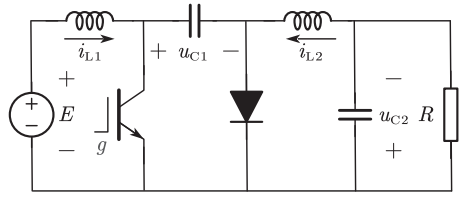

Fig. 7. Topology of cuk converters.

capacitor voltage is given in the following:

$$\begin{array}{cc|cc} \text{Freewheeling} & \text{Trend} & L\frac{di_L}{dt} & C\frac{du_C}{dt} \\ i_L > 0 & -u_C > 0 & -u_C & i_L - \frac{u_C}{R} \\ i_L > 0 & -u_C \leqslant 0 & -u_C & i_L - \frac{u_C}{R} \\ i_L = 0 & -u_C > 0 & -u_C & i_L - \frac{u_C}{R} \\ i_L = 0 & -u_C \leqslant 0 & 0 & i_L - \frac{u_C}{R}. \end{array} \tag{6}$$

Similar to the derivation in (4), $L\frac{di_L}{dt}$ can be expressed as $\eta_2(-u_C)$ when $g = 0$. The simplification process for η_2 mirrors that of (5), and thus the derivation is omitted. The state descriptor η_2 is shown in the following:

$$\eta_2 = (i_L > 0) \vee (u_C < 0) \tag{7}$$

Summarizing the above analysis and derivations, the model of the buck converter can be expressed as

$$\begin{bmatrix} L\frac{di_L}{dt} \\ C\frac{du_C}{dt} \end{bmatrix} = \begin{bmatrix} \eta_1 (E - u_c) & -\eta_2 u_C \\ i_L - \frac{u_C}{R} & i_L - \frac{u_C}{R} \end{bmatrix} \begin{bmatrix} g \\ 1 - g \end{bmatrix}. \tag{8}$$

From (8), it is evident that whenever the inductor current i_L reaches 0 and continues to decrease, the state descriptors η_1 and η_2 will enforce the circuit to transition to a state where the trend of inductor current is 0, effectively preventing i_L from becoming negative. Thus, the model incorporating state descriptors is in strict accordance with the physical model.

B. State Quadrant Modeling: Cuk Converter

The topology of the cuk converter is shown in Fig. 7. Unlike single-inductor converters, the cuk converter features two inductors. The key distinction between CCM and DCM in this converter is determined by whether the sum of i_{L1} and i_{L2} is continuous. Therefore, when defining the state quadrants, the division is based on whether $\sum_{i=1}^{2} i_{Li}$ is 0 and the trend of $\sum_{i=1}^{2} i_{Li}$.

When $g = 1$, the freewheeling axis is divided into two cases: $\sum_{i=1}^{2} i_{Li} > 0$ and $\sum_{i=1}^{2} i_{Li} = 0$. The trend of the sum of the inductor currents is determined by $\frac{E}{L_1} + \frac{u_{C1}-u_{C2}}{L_2}$. This expression can be decomposed into two parts: $\frac{E}{L_1}$ represents the trend of i_{L1}, and $\frac{u_{C1}-u_{C2}}{L_2}$ represents the trend of i_{L2}. The state quadrants are shown in Fig. 8. Whether in CCM or DCM, the capacitor current relationships $C_1\frac{du_{C1}}{dt} = -i_{L2}$ and $C_2\frac{du_{C2}}{dt} = i_{L2} - \frac{u_{C2}}{R}$ always hold. We focus on analyzing the inductor currents.

1) *Quadrant I* $\Leftrightarrow \sum_{i=1}^{2} i_{Li} > 0$ *and* $\frac{E}{L_1} > \frac{u_{C2}-u_{C1}}{L_2}$: Due to $\sum_{i=1}^{2} i_{Li} > 0$, the inductor's freewheeling function causes the switch to conduct. Therefore, $L_1\frac{di_{L1}}{dt} = E$ and $L_2\frac{di_{L2}}{dt} = u_{C1} - u_{C2}$.

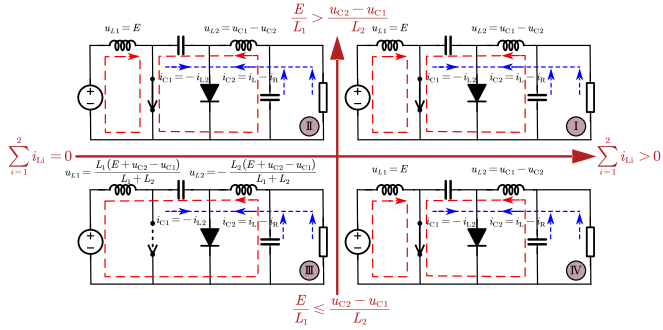

Fig. 8. State quadrant analysis of the cuk converter ($g = 1$).

2) *Quadrant II* $\Leftrightarrow \sum_{i=1}^{2} i_{Li} = 0$ *and* $\frac{E}{L_1} > \frac{u_{C2}-u_{C1}}{L_2}$: The trend of the sum of the inductor currents, $\frac{E}{L_1} + \frac{u_{C1}-u_{C2}}{L_2}$, is positive, which leads to an increase in the sum of the inductor currents. This prevents the switch from entering reverse cutoff. Consequently, $L_1\frac{di_{L1}}{dt}$ and $L_2\frac{di_{L2}}{dt}$ are E and $u_{C1} - u_{C2}$, respectively.
3) *Quadrant III* $\Leftrightarrow \sum_{i=1}^{2} i_{Li} = 0$ *and* $\frac{E}{L_1} \leqslant \frac{u_{C2}-u_{C1}}{L_2}$: The trend of the sum of the inductor currents, $\frac{E}{L_1} + \frac{u_{C1}-u_{C2}}{L_2}$, is negative, leading to a decrease in the sum of the inductor currents. This situation triggers the reverse cutoff of the switch. Consequently, the voltages across the two inductors depend on the loop formed by the power source, capacitor 1, capacitor 2, inductor 1, and inductor 2. Therefore, $L_1\frac{di_{L1}}{dt}$ and $L_2\frac{di_{L2}}{dt}$ are given by $\frac{L_1(E+u_{C2}-u_{C1})}{L_1+L_2}$ and $-\frac{L_2(E+u_{C2}-u_{C1})}{L_1+L_2}$, respectively.
4) *Quadrant IV* $\Leftrightarrow \sum_{i=1}^{2} i_{Li} > 0$ *and* $\frac{E}{L_1} \leqslant \frac{u_{C2}-u_{C1}}{L_2}$: The switch remains conductive because $\sum_{i=1}^{2} i_{Li} > 0$. In this case, $L_1\frac{di_{L1}}{dt} = E$ and $L_2\frac{di_{L2}}{dt} = u_{C1} - u_{C2}$.

When $g = 1$, the logical expressions and differential equations corresponding to the four state quadrants of the cuk converter are shown in (13) shown at the bottom of the next page. The derivation of the unified differential equations for the cuk converter when $g = 1$ follows a similar process to that in (4) and (5), and is therefore not reiterated here. These equations are presented in the following:

$$\begin{cases} L_1\frac{di_{L1}}{dt} = \eta_1 E + (1 - \eta_1) Q_1 \\ C_1\frac{du_{C1}}{dt} = -i_{L2} \\ L_2\frac{di_{L2}}{dt} = \eta_1 (u_{C1} - u_{C2}) + (1 - \eta_1) Q_2 \\ C_2\frac{du_{C2}}{dt} = i_{L2} - \frac{u_{C2}}{R} \end{cases} \tag{9}$$

where

$$\begin{aligned} \eta_1 &= \left[\left(\sum_{i=1}^{2} i_{Li}\right) > 0\right] \vee \left[\left(\frac{E}{L_1} + \frac{u_{C1}-u_{C2}}{L_2}\right) > 0\right] \\ Q_1 &= \frac{L_1(E+u_{C2}-u_{C1})}{L_1+L_2}, Q_2 = -\frac{L_2(E+u_{C2}-u_{C1})}{L_1+L_2}. \end{aligned} \tag{10}$$

Similarly, we can analyze the state quadrants of the cuk converter when $g = 0$, as shown in Fig. 9. The logical expressions and differential equations corresponding to each quadrant are shown in (14), shown at the bottom of this page. By following the derivation process in (4) and (5), we obtain the unified

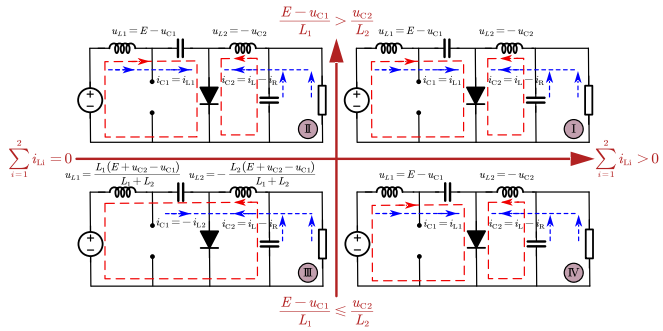

Fig. 9. State quadrant analysis of the cuk converter ($g = 0$).

differential equations when $g = 0$, as shown in the following:

$$\begin{cases} L_1 \frac{di_{L1}}{dt} = \eta_2 \left(E - u_{C1}\right) + \left(1 - \eta_2\right) Q_1 \\ C_1 \frac{du_{C1}}{dt} = i_{L1} \\ L_2 \frac{di_{L2}}{dt} = -\eta_2 u_{C2} + \left(1 - \eta_2\right) Q_2 \\ C_2 \frac{du_{C2}}{dt} = i_{L2} - \frac{u_{C2}}{R} \end{cases} \tag{11}$$

where $\eta_2 = [(\sum_{i=1}^{2} i_{Li}) > 0] \vee [(\frac{E-u_{C1}}{L_1} + \frac{-u_{C2}}{L_2}) > 0]$.

Summarizing the equations for $g = 1$ and $g = 0$, the model of the cuk converter is given in the following:

$$\begin{bmatrix} L_1 \frac{di_{L1}}{dt} \\ C_1 \frac{du_{C1}}{dt} \\ L_2 \frac{di_{L2}}{dt} \\ C_2 \frac{du_{C2}}{dt} \end{bmatrix} = \begin{bmatrix} \eta_1 E + \left(1 - \eta_1\right) Q_1 \\ -i_{L2} \\ \eta_1 \left(u_{C1} - u_{C2}\right) + \left(1 - \eta_1\right) Q_2 \\ i_{L2} - \frac{u_{C2}}{R} \end{bmatrix} g + \begin{bmatrix} \eta_2 \left(E - u_{C1}\right) + \left(1 - \eta_2\right) Q_1 \\ i_{L1} \\ -\eta_2 u_{C2} + \left(1 - \eta_2\right) Q_2 \\ i_{L2} - \frac{u_{C2}}{R} \end{bmatrix} (1 - g) \tag{12}$$

C. Standard Process and Extension of the State Quadrant Modeling Approach

The modeling framework described above can be extended to other dc–dc converters. To facilitate the use of this modeling approach, we have standardized the modeling process using the state quadrant modeling approach, as follows.

1) *Step 1:* Identify the state quadrants:
   1) The current that marks the operating mode (CCM or DCM) of the converter is identified and defined as the characteristic current i_{key}. For single-inductor converters, i_{key} is the inductor current. For dual-inductor converters, i_{key} is the sum of the inductor currents.
   2) The freewheeling axis is divided into two states: freewheeling ($i_{\text{key}} \neq 0$) and boundary ($i_{\text{key}} = 0$).
   3) The trend axis is divided into positive and negative trends. The trend of i_{key} is calculated by assuming that the inductor is freewheeling and determining the inductor voltage u_{L}. For single-inductor converters, the trend is given by $\frac{u_{\text{L}}}{L}$. For dual-inductor converters, the trend is given by $\frac{u_{\text{L1}}}{L_1} + \frac{u_{\text{L2}}}{L_2}$.
   4) Combine the states of the freewheeling axis and the trend axis to obtain all possible state quadrants.
2) *Step 2:* Construct the state descriptors.
   1) The conduction condition of switches and diodes can be determined by the freewheeling state and trend of i_{key}, thereby determining the operating mode of the converter in each quadrant.
   2) Organize the logical information and differential equations for each quadrant into a structured table. The first to fourth columns represent freewheeling logic, trend logic, differential equations for the inductor current, and differential equations for the capacitor voltage, respectively.
   3) The unified differential equations for the inductor current and capacitor voltage can be expressed as the sum of products of logical expressions and differential equations, as follows:

$$\begin{aligned} L \frac{di_{\text{L}}}{dt} &= \sum\nolimits_i \left(\hat{L}_{\text{i}} \left(i_{\text{key}}\right) \wedge \check{L}_{\text{i}} \left(i_{\text{key}}\right)\right) \cdot \hat{D}_{\text{i}} \left(E, u_{\text{C}}\right) \\ C \frac{du_{\text{C}}}{dt} &= \sum\nolimits_i \left(\hat{L}_{\text{i}} \left(i_{\text{key}}\right) \wedge \check{L}_{\text{i}} \left(i_{\text{key}}\right)\right) \cdot \check{D}_{\text{i}} \left(i_{\text{L}}, i_{\text{load}}\right) \end{aligned} \tag{15}$$

Freewheeling Axis	Trend Axis	$L_1 \frac{di_{L1}}{dt}$	$C_1 \frac{du_{C1}}{dt}$	$L_2 \frac{di_{L2}}{dt}$	$C_2 \frac{du_{C2}}{dt}$
$\sum_{i=1}^{2} i_{\text{Li}} > 0$	$\left(\frac{E}{L_1} + \frac{u_{C1}-u_{C2}}{L_2}\right) > 0$	E	$-i_{L2}$	$u_{C1} - u_{C2}$	$i_{L2} - \frac{u_{C2}}{R}$
$\sum_{i=1}^{2} i_{\text{Li}} = 0$	$\left(\frac{E}{L_1} + \frac{u_{C1}-u_{C2}}{L_2}\right) > 0$	E	$-i_{L2}$	$u_{C1} - u_{C2}$	$i_{L2} - \frac{u_{C2}}{R}$
$\sum_{i=1}^{2} i_{\text{Li}} = 0$	$\left(\frac{E}{L_1} + \frac{u_{C1}-u_{C2}}{L_2}\right) \leqslant 0$	$\frac{L_1(E+u_{C2}-u_{C1})}{L_1+L_2}$	$-i_{L2}$	$-\frac{L_2(E+u_{C2}-u_{C1})}{L_1+L_2}$	$i_{L2} - \frac{u_{C2}}{R}$
$\sum_{i=1}^{2} i_{\text{Li}} > 0$	$\left(\frac{E}{L_1} + \frac{u_{C1}-u_{C2}}{L_2}\right) \leqslant 0$	E	$-i_{L2}$	$u_{C1} - u_{C2}$	$i_{L2} - \frac{u_{C2}}{R}$

(13)

Freewheeling Axis	Trend Axis	$L_1 \frac{di_{L1}}{dt}$	$C_1 \frac{du_{C1}}{dt}$	$L_2 \frac{di_{L2}}{dt}$	$C_2 \frac{du_{C2}}{dt}$
$\sum_{i=1}^{2} i_{\text{Li}} > 0$	$\left(\frac{E-u_{C1}}{L_1} + \frac{-u_{C2}}{L_2}\right) > 0$	$E - u_{C1}$	i_{L1}	$-u_{C2}$	$i_{L2} - \frac{u_{C2}}{R}$
$\sum_{i=1}^{2} i_{\text{Li}} = 0$	$\left(\frac{E-u_{C1}}{L_1} + \frac{-u_{C2}}{L_2}\right) > 0$	$E - u_{C1}$	i_{L1}	$-u_{C2}$	$i_{L2} - \frac{u_{C2}}{R}$
$\sum_{i=1}^{2} i_{\text{Li}} = 0$	$\left(\frac{E-u_{C1}}{L_1} + \frac{-u_{C2}}{L_2}\right) \leqslant 0$	$\frac{L_1(E+u_{C2}-u_{C1})}{L_1+L_2}$	i_{L1}	$-\frac{L_2(E+u_{C2}-u_{C1})}{L_1+L_2}$	$i_{L2} - \frac{u_{C2}}{R}$
$\sum_{i=1}^{2} i_{\text{Li}} > 0$	$\left(\frac{E-u_{C1}}{L_1} + \frac{-u_{C2}}{L_2}\right) \leqslant 0$	$E - u_{C1}$	i_{L1}	$-u_{C2}$	$i_{L2} - \frac{u_{C2}}{R}$.

(14)

TABLE I
STATE QUADRANT MODELING FOR TYPICAL DC–DC CONVERTERS

Single-inductor Converter	**Buck** $\begin{bmatrix} L\frac{di_L}{dt} \\ C\frac{du_C}{dt} \end{bmatrix} = \begin{bmatrix} \eta_1(E-u_C) & -\eta_2 u_C \\ i_L - \frac{u_C}{R} & i_L - \frac{u_C}{R} \end{bmatrix} \begin{bmatrix} g \\ 1-g \end{bmatrix}$ $\eta_1 = (i_L > 0) \vee (E > u_C)$ $\eta_2 = (i_L > 0) \vee (u_C < 0)$	**Boost** $\begin{bmatrix} L\frac{di_L}{dt} \\ C\frac{du_C}{dt} \end{bmatrix} = \begin{bmatrix} E & \eta_1(E-u_C) \\ -\frac{u_C}{R} & \eta_2 i_L - \frac{u_C}{R} \end{bmatrix} \begin{bmatrix} g \\ 1-g \end{bmatrix}$ $\eta_1 = (i_L > 0) \vee (E > u_C)$ $\eta_2 = (i_L > 0)$	**Buck-Boost** $\begin{bmatrix} L\frac{di_L}{dt} \\ C\frac{du_C}{dt} \end{bmatrix} = \begin{bmatrix} E & -\eta u_C \\ -\frac{u_C}{R} & \eta i_L - \frac{u_C}{R} \end{bmatrix} \begin{bmatrix} g \\ 1-g \end{bmatrix}$ $\eta = (i_L > 0) \vee (u_C \leqslant 0)$
Dual-inductor Converter	**Cuk** $\begin{bmatrix} L_1\frac{di_{L1}}{dt} \\ C_1\frac{du_{C1}}{dt} \\ L_2\frac{di_{L2}}{dt} \\ C_2\frac{du_{C2}}{dt} \end{bmatrix} = \begin{bmatrix} \eta_1 E + (1-\eta_1)Q_1 & \eta_2(E-u_{C1}) + (1-\eta_2)Q_1 \\ -i_{L2} & i_{L1} \\ \eta_1(u_{C1}-u_{C2}) + (1-\eta_1)Q_2 & -\eta_2 u_{C2} + (1-\eta_2)Q_2 \\ i_{L2} - \frac{u_{C2}}{R} & i_{L2} - \frac{u_{C2}}{R} \end{bmatrix} \begin{bmatrix} g \\ 1-g \end{bmatrix}$ $\eta_1 = [(\sum_{i=1}^{2} i_{Li}) > 0] \vee \left[\left(\frac{E}{L_1} + \frac{u_{C1}-u_{C2}}{L_2}\right) > 0\right], Q_1 = \frac{L_1(E+u_{C2}-u_{C1})}{L_1+L_2}$ $\eta_2 = [(\sum_{i=1}^{2} i_{Li}) > 0] \vee \left[\left(\frac{E-u_{C1}}{L_1} + \frac{-u_{C2}}{L_2}\right) > 0\right], Q_2 = -\frac{L_2(E+u_{C2}-u_{C1})}{L_1+L_2}$	**Zeta** $\begin{bmatrix} L_1\frac{di_{L1}}{dt} \\ C_1\frac{du_{C1}}{dt} \\ L_2\frac{di_{L2}}{dt} \\ C_2\frac{du_{C2}}{dt} \end{bmatrix} = \begin{bmatrix} \eta_1 E + (1-\eta_1)Q_1 & \eta_2(-u_{C1}) + (1-\eta_2)Q_1 \\ -i_{L2} & i_{L1} \\ \eta_1(E+u_{C1}-u_{C2}) + (1-\eta_1)Q_2 & -\eta_2 u_{C2} + (1-\eta_2)Q_2 \\ i_{L2} - \frac{u_{C2}}{R} & i_{L2} - \frac{u_{C2}}{R} \end{bmatrix} \begin{bmatrix} g \\ 1-g \end{bmatrix}$ $\eta_1 = [(\sum_{i=1}^{2} i_{Li}) > 0] \vee \left[\left(\frac{E}{L_1} + \frac{E+u_{C1}-u_{C2}}{L_2}\right) > 0\right], Q_1 = \frac{L_1(u_{C2}-u_{C1})}{L_1+L_2}$ $\eta_2 = [(\sum_{i=1}^{2} i_{Li}) > 0] \vee \left[\left(\frac{-u_{C1}}{L_1} + \frac{-u_{C2}}{L_2}\right) > 0\right], Q_2 = -\frac{L_2(u_{C2}-u_{C1})}{L_1+L_2}$	**Sepic** $\begin{bmatrix} L_1\frac{di_{L1}}{dt} \\ C_1\frac{du_{C1}}{dt} \\ L_2\frac{di_{L2}}{dt} \\ C_2\frac{du_{C2}}{dt} \end{bmatrix} = \begin{bmatrix} \eta_1 E + (1-\eta_1)Q_1 & \eta_2(E-u_{C1}-u_{C2}) + (1-\eta_2)Q_1 \\ -i_{L2} & i_{L1} \\ \eta_1 u_{C1} + (1-\eta_1)Q_2 & -\eta_2 u_{C2} + (1-\eta_2)Q_2 \\ -\frac{u_{C2}}{R} & i_{L1} + i_{L2} - \frac{u_{C2}}{R} \end{bmatrix} \begin{bmatrix} g \\ 1-g \end{bmatrix}$ $\eta_1 = [(\sum_{i=1}^{2} i_{Li}) > 0] \vee \left[\left(\frac{E}{L_1} + \frac{u_{C1}}{L_2}\right) > 0\right], Q_1 = \frac{L_1(E-u_{C1})}{L_1+L_2}$ $\eta_2 = [(\sum_{i=1}^{2} i_{Li}) > 0] \vee \left[\left(\frac{E-u_{C1}-u_{C2}}{L_1} + \frac{-u_{C2}}{L_2}\right) > 0\right], Q_2 = -\frac{L_2(E-u_{C1})}{L_1+L_2}$
Multiphase Converter	**Buck** $\begin{cases} L_i\frac{di_{Li}}{dt} = \begin{pmatrix} \eta_{1i}(E-u_C)g_i + \\ \eta_{2i}(-u_C)(1-g_i) \end{pmatrix} \\ C\frac{du_C}{dt} = \sum_{i=a}^{c} i_{Li} - \frac{u_C}{R} \\ \eta_{1i} = (i_{Li} > 0) \vee (E > u_C) \\ \eta_{2i} = (i_{Li} > 0) \vee (u_C < 0) \\ i = a, b, c \end{cases}$	**Boost** $\begin{cases} L_i\frac{di_{Li}}{dt} = \begin{pmatrix} E \cdot g_i + \\ \eta_{1i}(E-u_C)(1-g_i) \end{pmatrix} \\ C\frac{du_C}{dt} = \sum_{i=a}^{c} \eta_{2i} \cdot i_{Li} \cdot (1-g_i) - \frac{u_C}{R} \\ \eta_{1i} = (i_{Li} > 0) \vee (E > u_C) \\ \eta_{2i} = (i_{Li} > 0) \\ i = a, b, c \end{cases}$	**Buck-boost** $\begin{cases} L_i\frac{di_{Li}}{dt} = \begin{pmatrix} E \cdot g_i + \\ \eta_i(-u_C)(1-g_i) \end{pmatrix} \\ C\frac{du_C}{dt} = \sum_{i=a}^{c} \eta_i \cdot i_{Li} \cdot (1-g_i) - \frac{u_C}{R} \\ \eta_i = (i_{Li} > 0) \vee (u_C \leqslant 0) \\ i = a, b, c \end{cases}$
Isolated Converter	**Forward** $\begin{bmatrix} L\frac{di_L}{dt} \\ C\frac{du_C}{dt} \end{bmatrix} = \begin{bmatrix} \eta_1\left(\frac{N_2E}{N_1} - u_C\right) & -\eta_2 u_C \\ i_L - \frac{u_C}{R} & i_L - \frac{u_C}{R} \end{bmatrix} \begin{bmatrix} g \\ 1-g \end{bmatrix}$ $\eta_1 = (i_L > 0) \vee \left(\frac{N_2E}{N_1} > u_C\right), \eta_2 = (i_L > 0) \vee (u_C < 0)$	**Push-Pull** $\begin{bmatrix} L\frac{di_L}{dt} \\ C\frac{du_C}{dt} \end{bmatrix} = \begin{bmatrix} -\eta_1 u_C & \eta_2\left(\frac{N_2E}{N_1} - u_C\right) & \eta_2\left(\frac{N_2E}{N_1} - u_C\right) & -\eta_1 u_C \\ i_L - \frac{u_C}{R} & i_L - \frac{u_C}{R} & i_L - \frac{u_C}{R} & i_L - \frac{u_C}{R} \end{bmatrix} \begin{bmatrix} (1-g_1)(1-g_2) \\ g_1(1-g_2) \\ (1-g_1)g_2 \\ g_1 g_2 \end{bmatrix}$ $\eta_1 = (i_L > 0) \vee (u_C < 0), \eta_2 = (i_L > 0) \vee \left(\frac{N_2E}{N_1} > u_C\right)$
	Flyback $\begin{bmatrix} \frac{d\phi}{dt} \\ C\frac{du_C}{dt} \end{bmatrix} = \begin{bmatrix} \frac{E}{N_1} & -\eta\frac{u_C}{N_2} \\ -\frac{u_C}{R} & \eta\frac{N_1^2\phi}{N_2 L_m} - \frac{u_C}{R} \end{bmatrix} \begin{bmatrix} g \\ 1-g \end{bmatrix}$ $\eta = (\phi > 0) \vee (u_C \leqslant 0)$	**Full-Bridge** $\begin{bmatrix} L\frac{di_L}{dt} \\ C\frac{du_C}{dt} \end{bmatrix} = \begin{bmatrix} -\eta_1 u_C & \eta_2\left(\frac{N_2E}{N_1} - u_C\right) & \eta_2\left(\frac{N_2E}{N_1} - u_C\right) \\ i_L - \frac{u_C}{R} & i_L - \frac{u_C}{R} & i_L - \frac{u_C}{R} \end{bmatrix} \begin{bmatrix} g_1 g_2 \\ g_1(1-g_2) \\ (1-g_1)g_2 \end{bmatrix}$ $\eta_1 = (i_L > 0) \vee (u_C < 0), \eta_2 = (i_L > 0) \vee \left(\frac{N_2E}{N_1} > u_C\right)$	

where $\hat{L}_{\mathrm{i}}(i_{\mathrm{key}})$ is the freewheeling logical expression, $\check{L}_{\mathrm{i}}(i_{\mathrm{key}})$ is the trend logical expression, $\hat{D}_{\mathrm{i}}(E, u_{\mathrm{C}})$ is the inductor differential equation, and $\check{D}_{\mathrm{i}}(i_{\mathrm{L}}, i_{\mathrm{load}})$ is the capacitor differential equation from the ith row of the table in Step 2.

4) Use logical operations, such as commutativity and absorption, to simplify the logical expressions as much as possible, thereby obtaining the state descriptors.

3) *Step 3:* After simplifying the state descriptors, the differential equations under different switching states are unified into the form $\dot{\boldsymbol{x}} = f(\boldsymbol{x}, \boldsymbol{u})$.

Our modeling approach is applicable to a wide range of classical dc–dc converters. The converters modeled using the state quadrant approach in this article are as follows:

1) *Single-inductor converters:* Buck converter, boost converter, and buck–boost converter.
2) *Dual-inductor converters:* Cuk converter, zeta converter, and sepic converter.
3) *Multiphase converters:* Multiphase buck converter, multiphase boost converter, and multiphase buck–boost converter.
4) *Isolated converters:* Forward converter, flyback converter, push–pull converter, and full-bridge converter.

Due to page limitations, the derivation of the models for the aforementioned converters is provided in the *Supplementary File*. This article presents the final models in Table I, with corresponding topologies in Appendix A.

The models presented in Table I correspond to the unidirectional versions of the converters. The proposed method can be extended to bidirectional versions. Bidirectional converters allow for bidirectional current flow, which is always consistent with the assumptions of the CCM models. Therefore, *for any bidirectional version of these converters, the mathematical model can be derived by setting the state descriptors in the corresponding model to 1.* For example, by setting η_1 and η_2 to 1 in the buck converter model, the model for the bidirectional buck converter with complementary conduction can be obtained.

The aforementioned models are switch models, which take the switch signal g as the input. They are compatible with control strategies that employ switch signals as input. By applying existing averaging methods to the switch models, average models can be obtained, which take duty cycle as input. For instance, replacing g with d and $1-g$ with $1-d$ in the switch model of buck converters yields the corresponding average model. These

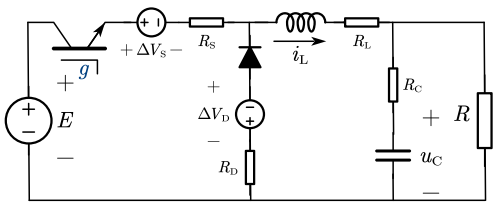

Fig. 10. Equivalent circuit of buck converter considering nonideal factors.

average models are suitable for control methods that utilize duty cycle as input.

D. Incorporating Nonideal Factors in Modeling

Designing controllers based on models that omit nonideal factors is a common practice, and the prior models are sufficient for this purpose. The state quadrant modeling method can also handle converters with nonideal factors. This section explores this application preliminarily.

The buck converter's equivalent circuit with nonideal factors is shown in Fig. 10. It includes the switch's voltage drop ΔV_{S} and resistance R_{S}, the diode's voltage drop ΔV_{D} and resistance R_{D}, and the inductor's and capacitor's parasitic resistances R_{L} and R_{C}.

First, we derive the equations for $g = 1$. Following the first step of the standard process, the freewheeling axis is divided into two states: freewheeling ($i_{\mathrm{L}} = 0$) and boundary ($i_{\mathrm{L}} = 0$). The trend axis is divided into $y_1 > 0$ and $y_1 \leqslant 0$. Here, y_1 is the inductor voltage under the freewheeling condition, as given in (16). By combining these divisions, we obtain all the state quadrants.

$$L\frac{di_{\mathrm{L}}}{dt} = \underbrace{E - u_{\mathrm{C}} - (R_{\mathrm{S}} + R_{\mathrm{L}})\, i_{\mathrm{L}} - R_{\mathrm{C}}\frac{i_{\mathrm{L}} - \frac{u_{\mathrm{C}}}{R}}{1 + \frac{R_{\mathrm{C}}}{R}} - \Delta V_{\mathrm{S}}}_{y_1}. \tag{16}$$

Following the second step of the standard procedure, we derive the differential equations for each state quadrant and organize them into a table, as shown in (17). These equations are then expressed in a unified form, as shown in (18). We simplify the state descriptor η_1 [similar to (5)] to obtain its simplest form, as shown in (19)

Freewheeling	Trend	$L\frac{di_{\mathrm{L}}}{dt}$	$C\frac{du_{\mathrm{C}}}{dt}$
$i_{\mathrm{L}} > 0$	$y_1 > 0$	y_1	$\left(i_{\mathrm{L}} - \frac{u_{\mathrm{C}}}{R}\right) / \left(1 + \frac{R_{\mathrm{C}}}{R}\right)$
$i_{\mathrm{L}} > 0$	$y_1 \leqslant 0$	y_1	$\left(i_{\mathrm{L}} - \frac{u_{\mathrm{C}}}{R}\right) / \left(1 + \frac{R_{\mathrm{C}}}{R}\right)$
$i_{\mathrm{L}} = 0$	$y_1 > 0$	y_1	$\left(i_{\mathrm{L}} - \frac{u_{\mathrm{C}}}{R}\right) / \left(1 + \frac{R_{\mathrm{C}}}{R}\right)$
$i_{\mathrm{L}} = 0$	$y_1 \leqslant 0$	0	$\left(i_{\mathrm{L}} - \frac{u_{\mathrm{C}}}{R}\right) / \left(1 + \frac{R_{\mathrm{C}}}{R}\right)$

(17)

$$\begin{cases} L\frac{di_{\mathrm{L}}}{dt} = \eta_1 \cdot y_1 \\ C\frac{du_{\mathrm{C}}}{dt} = \frac{i_{\mathrm{L}} - \frac{u_{\mathrm{C}}}{R}}{1 + \frac{R_{\mathrm{C}}}{R}} \end{cases} \tag{18}$$

$$\eta_1 = (i_{\mathrm{L}} > 0) \vee (y_1 > 0)\,. \tag{19}$$

Similarly to the process from (17) to (19), the equations for $g = 0$ can be derived, as shown in the following:

$$\begin{cases} L\frac{di_{\mathrm{L}}}{dt} = \eta_2 \cdot y_2 \\ C\frac{du_{\mathrm{C}}}{dt} = \frac{i_{\mathrm{L}} - \frac{u_{\mathrm{C}}}{R}}{1 + \frac{R_{\mathrm{C}}}{R}} \end{cases} \tag{20}$$

where

$$\begin{aligned} y_2 &= -u_{\mathrm{C}} - (R_{\mathrm{D}} + R_{\mathrm{L}})\, i_{\mathrm{L}} - R_{\mathrm{C}}\frac{i_{\mathrm{L}} - \frac{u_{\mathrm{C}}}{R}}{1 + \frac{R_{\mathrm{C}}}{R}} - \Delta V_{\mathrm{D}} \\ \eta_2 &= (i_{\mathrm{L}} > 0) \vee (y_2 > 0)\,. \end{aligned} \tag{21}$$

Following the third step of the standard procedure, we derive the Buck converter model with nonideal factors, as shown in the following:

$$\begin{bmatrix} L\frac{di_{\mathrm{L}}}{dt} \\ C\frac{du_{\mathrm{C}}}{dt} \end{bmatrix} = \begin{bmatrix} \eta_1 \cdot y_1 & \eta_2 \cdot y_2 \\ \frac{i_{\mathrm{L}} - \frac{u_{\mathrm{C}}}{R}}{1 + \frac{R_{\mathrm{C}}}{R}} & \frac{i_{\mathrm{L}} - \frac{u_{\mathrm{C}}}{R}}{1 + \frac{R_{\mathrm{C}}}{R}} \end{bmatrix} \begin{bmatrix} g \\ 1 - g \end{bmatrix} \tag{22}$$

where y_1, η_1, y_2, and η_2 are given in (16), (19), and (21).

IV. Numerical Solution of State Quadrant Model

The models can be solved using classical numerical methods despite containing logical variables. The Forward Euler, fourth-order Runge–Kutta, backward Euler, and trapezoidal Euler methods are applied to the proposed buck converter model to demonstrate compatibility with classical solvers.

A. Forward Euler Method

The proposed model is discretized using the forward Euler method, yielding the discrete equation shown in the following:

$$\begin{bmatrix} i_{\mathrm{L}}^{k+1} \\ u_{\mathrm{C}}^{k+1} \end{bmatrix} = \begin{bmatrix} i_{\mathrm{L}}^{k} \\ u_{\mathrm{C}}^{k} \end{bmatrix} + \Delta t \cdot f\left(\begin{bmatrix} i_{\mathrm{L}}^{k} \\ u_{\mathrm{C}}^{k} \end{bmatrix}, g^k\right) \tag{23}$$

where $f(\cdot,\cdot)$ is defined as follows:

$$\begin{cases} f\left(\begin{bmatrix} i_{\mathrm{L}} \\ u_{\mathrm{C}} \end{bmatrix}, g\right) = \begin{bmatrix} \eta_1 \cdot (E - u_{\mathrm{C}}) & -\eta_2 \cdot u_{\mathrm{C}} \\ i_{\mathrm{L}} - \frac{u_{\mathrm{C}}}{R} & i_{\mathrm{L}} - \frac{u_{\mathrm{C}}}{R} \end{bmatrix} \begin{bmatrix} g \\ 1 - g \end{bmatrix} \\ \eta_1 = (i_{\mathrm{L}} > 0) \vee (E > u_{\mathrm{C}}) \\ \eta_2 = (i_{\mathrm{L}} > 0) \vee (u_{\mathrm{C}} < 0)\,. \end{cases} \tag{24}$$

Beginning from time zero, the solution at each time step can be computed by iteratively applying (23).

B. Fourth-order Runge–Kutta Method

The proposed model is discretized using the fourth-order Runge–Kutta method, yielding the discrete equation shown in the following:

$$\begin{bmatrix} i_{\mathrm{L}}^{k+1} \\ u_{\mathrm{C}}^{k+1} \end{bmatrix} = \begin{bmatrix} i_{\mathrm{L}}^{k} \\ u_{\mathrm{C}}^{k} \end{bmatrix} + \frac{\Delta t}{6}(k_1 + 2k_2 + 2k_3 + k_4) \tag{25}$$

where k_1, k_2, k_3, and k_4 are defined as follows:

$$k_1 = f\left(\begin{bmatrix} i_{\mathrm{L}}^{k} \\ u_{\mathrm{C}}^{k} \end{bmatrix}, g^k\right), \quad k_2 = f\left(\begin{bmatrix} i_{\mathrm{L}}^{k} \\ u_{\mathrm{C}}^{k} \end{bmatrix} + \frac{1}{2}k_1, g^k\right)$$

$$k_3 = f\left(\begin{bmatrix} i_{\mathrm{L}}^k \\ u_{\mathrm{C}}^k \end{bmatrix} + \frac{1}{2}k_2, g^k\right), \quad k_4 = f\left(\begin{bmatrix} i_{\mathrm{L}}^k \\ u_{\mathrm{C}}^k \end{bmatrix} + k_3, g^k\right). \tag{26}$$

C. Backward Euler Method

The proposed model is discretized using the backward Euler method, yielding the discrete equation shown in the following:

$$\begin{bmatrix} i_{\mathrm{L}}^{k+1} \\ u_{\mathrm{C}}^{k+1} \end{bmatrix} = \begin{bmatrix} i_{\mathrm{L}}^k \\ u_{\mathrm{C}}^k \end{bmatrix} + \Delta t \cdot f\left(\begin{bmatrix} i_{\mathrm{L}}^{k+1} \\ u_{\mathrm{C}}^{k+1} \end{bmatrix}, g^k\right). \tag{27}$$

Both sides of (27) contain the term $[i_{\mathrm{L}}^{k+1}, u_{\mathrm{C}}^{k+1}]^T$, making it impossible to directly derive an iterative equation from k to $k+1$. Since (27) represents a nonlinear algebraic system involving logical variables, it is necessary to employ nonlinear algebraic equation solvers to obtain the solution at time step $k+1$. However, such nonlinear algebraic equation solvers are computationally inefficient.

To overcome this issue, we propose a novel method that combines matrix inversion with a posteriori verification. Initially, a value for the logical variables at time step $k+1$ is assumed. Based on this assumption, the solution is obtained through matrix inversion. Subsequently, the validity of the assumed logical variables is verified. If the assumption is correct, the derived solution is accepted; otherwise, the opposite value of the assumed logical variables is adopted, and matrix inversion is performed again. The detailed derivation is presented in the following.

When $g^k = 1$, (27) can be transformed into

$$\begin{bmatrix} i_{\mathrm{L}}^{k+1} \\ u_{\mathrm{C}}^{k+1} \end{bmatrix} = \Delta t \cdot A|_{\eta_1^{k+1}} \begin{bmatrix} i_{\mathrm{L}}^{k+1} \\ u_{\mathrm{C}}^{k+1} \end{bmatrix} + E\Delta t \cdot B|_{\eta_1^{k+1}} + \begin{bmatrix} i_{\mathrm{L}}^k \\ u_{\mathrm{C}}^k \end{bmatrix} \tag{28}$$

where

$$\begin{aligned} A|_\eta &= \begin{bmatrix} 0 & -\frac{\eta}{L} \\ \frac{1}{C} & -\frac{1}{CR} \end{bmatrix}, \; B|_\eta = \begin{bmatrix} \frac{\eta}{L} \\ 0 \end{bmatrix} \\ \eta_1^{k+1} &= \left(i_{\mathrm{L}}^{k+1} > 0\right) \vee \left(E > u_{\mathrm{C}}^{k+1}\right) \\ \eta_2^{k+1} &= \left(i_{\mathrm{L}}^{k+1} > 0\right) \vee \left(u_{\mathrm{C}}^{k+1} < 0\right). \end{aligned} \tag{29}$$

Simplifying (27) yields

$$\begin{bmatrix} i_{\mathrm{L}}^{k+1} \\ u_{\mathrm{C}}^{k+1} \end{bmatrix} = \left(I - \Delta t \cdot A|_{\eta_1^{k+1}}\right)^{-1} \left(E\Delta t \cdot B|_{\eta_1^{k+1}} + \begin{bmatrix} i_{\mathrm{L}}^k \\ u_{\mathrm{C}}^k \end{bmatrix}\right). \tag{30}$$

If $\eta_1^{k+1} = 1$, the preliminary solution for $\begin{bmatrix} i_{\mathrm{L}}^{k+1} \\ u_{\mathrm{C}}^{k+1} \end{bmatrix}$ is as follows:

$$\begin{bmatrix} \hat{i}_{\mathrm{L}}\big|_{\mathrm{g}=1} \\ \hat{u}_{\mathrm{C}}\big|_{\mathrm{g}=1} \end{bmatrix} = \left(I - \Delta t \cdot A|_1\right)^{-1} \left(E\Delta t \cdot B|_1 + \begin{bmatrix} i_{\mathrm{L}}^k \\ u_{\mathrm{C}}^k \end{bmatrix}\right). \tag{31}$$

The preliminary solution is valid if and only if $(\hat{i}_{\mathrm{L}}|_{\mathrm{g}=1} > 0) \vee (\hat{u}_{\mathrm{C}}|_{\mathrm{g}=1} > u_{\mathrm{C}}^{k+1})$ holds. If this condition is satisfied, then $\begin{bmatrix} i_{\mathrm{L}}^{k+1} \\ u_{\mathrm{C}}^{k+1} \end{bmatrix} = \begin{bmatrix} \hat{i}_{\mathrm{L}}|_{\mathrm{g}=1} \\ \hat{u}_{\mathrm{C}}|_{\mathrm{g}=1} \end{bmatrix}$. Otherwise, it indicates that $\eta_1^{k+1} = 0$, and thus

$$\begin{bmatrix} i_{\mathrm{L}}^{k+1} \\ u_{\mathrm{C}}^{k+1} \end{bmatrix} = \left(I - \Delta t \cdot A|_0\right)^{-1} \left(E\Delta t \cdot B|_0 + \begin{bmatrix} i_{\mathrm{L}}^k \\ u_{\mathrm{C}}^k \end{bmatrix}\right). \tag{32}$$

By combining the cases where the preliminary solution is valid and invalid, the iterative equation from step k to $k+1$ for $g = 1$ is obtained as follows:

$$\begin{aligned} \begin{bmatrix} i_{\mathrm{L}}^{k+1} \\ u_{\mathrm{C}}^{k+1} \end{bmatrix} = {} & \rho\Big|_{\mathrm{g}=1} \cdot \left(I - \Delta t \cdot A\Big|_1\right)^{-1} \left(E\Delta t \cdot B\Big|_1 + \begin{bmatrix} i_{\mathrm{L}}^k \\ u_{\mathrm{C}}^k \end{bmatrix}\right) \\ & + \bar{\rho}\Big|_{\mathrm{g}=1} \cdot \left(I - \Delta t \cdot A\Big|_0\right)^{-1} \left(E\Delta t \cdot B\Big|_0 + \begin{bmatrix} i_{\mathrm{L}}^k \\ u_{\mathrm{C}}^k \end{bmatrix}\right) \end{aligned} \tag{33}$$

where $\rho|_{\mathrm{g}=1} = (\hat{i}_{\mathrm{L}}|_{\mathrm{g}=1} > 0) \vee (E > \hat{u}_{\mathrm{C}}|_{\mathrm{g}=1})$ and $\bar{\rho}|_{\mathrm{g}=1} = 1 - \rho|_{\mathrm{g}=1}$.

When $g = 0$, a similar process yields

$$\begin{aligned} \begin{bmatrix} i_{\mathrm{L}}^{k+1} \\ u_{\mathrm{C}}^{k+1} \end{bmatrix} = {} & \rho|_{\mathrm{g}=0} \cdot \left(I - \Delta t \cdot A|_1\right)^{-1} \begin{bmatrix} i_{\mathrm{L}}^k \\ u_{\mathrm{C}}^k \end{bmatrix} \\ & + \bar{\rho}|_{\mathrm{g}=0} \cdot \left(I - \Delta t \cdot A|_0\right)^{-1} \begin{bmatrix} i_{\mathrm{L}}^k \\ u_{\mathrm{C}}^k \end{bmatrix} \end{aligned} \tag{34}$$

where $\rho|_{\mathrm{g}=0} = (\hat{i}_{\mathrm{L}}|_{\mathrm{g}=0} > 0) \vee (0 > \hat{u}_{\mathrm{C}}|_{\mathrm{g}=0})$, $\bar{\rho}|_{\mathrm{g}=0} = 1 - \rho|_{\mathrm{g}=0}$ and $\begin{bmatrix} \hat{i}_{\mathrm{L}}|_{\mathrm{g}=0} \\ \hat{u}_{\mathrm{C}}|_{\mathrm{g}=0} \end{bmatrix} = \left(I - \Delta t \cdot A|_1\right)^{-1} \begin{bmatrix} i_{\mathrm{L}}^k \\ u_{\mathrm{C}}^k \end{bmatrix}$.

Combining the iterative equations for $g = 1$ and $g = 0$, the final equations for solving the proposed model using the backward Euler method is given by

$$\begin{aligned} \begin{bmatrix} i_{\mathrm{L}}^{k+1} \\ u_{\mathrm{C}}^{k+1} \end{bmatrix} = {} & \begin{bmatrix} \rho|_{\mathrm{g}=0} \\ \bar{\rho}|_{\mathrm{g}=0} \end{bmatrix}^T \cdot \begin{bmatrix} \left(I - \Delta t \cdot A|_1\right)^{-1} \begin{bmatrix} i_{\mathrm{L}}^k \\ u_{\mathrm{C}}^k \end{bmatrix} \\ \left(I - \Delta t \cdot A|_0\right)^{-1} \begin{bmatrix} i_{\mathrm{L}}^k \\ u_{\mathrm{C}}^k \end{bmatrix} \end{bmatrix} \cdot \left(1 - g^k\right) \\ & + \begin{bmatrix} \rho|_{\mathrm{g}=1} \\ \bar{\rho}|_{\mathrm{g}=1} \end{bmatrix}^T \cdot \begin{bmatrix} \left(I - \Delta t \cdot A|_1\right)^{-1} \left(E\Delta t \cdot B|_1 + \begin{bmatrix} i_{\mathrm{L}}^k \\ u_{\mathrm{C}}^k \end{bmatrix}\right) \\ \left(I - \Delta t \cdot A|_0\right)^{-1} \left(E\Delta t \cdot B|_0 + \begin{bmatrix} i_{\mathrm{L}}^k \\ u_{\mathrm{C}}^k \end{bmatrix}\right) \end{bmatrix} \cdot g^k. \end{aligned} \tag{35}$$

D. Trapezoidal Euler Method

When the trapezoidal Euler method is applied to the proposed model, the following equation is obtained:

$$\begin{aligned} \begin{bmatrix} i_{\mathrm{L}}^{k+1} \\ u_{\mathrm{C}}^{k+1} \end{bmatrix} = {} & \begin{bmatrix} i_{\mathrm{L}}^k \\ u_{\mathrm{C}}^k \end{bmatrix} + \frac{\Delta t}{2} \cdot f\left(\begin{bmatrix} i_{\mathrm{L}}^k \\ u_{\mathrm{C}}^k \end{bmatrix}, g^k\right) \\ & + \frac{\Delta t}{2} \cdot f\left(\begin{bmatrix} i_{\mathrm{L}}^{k+1} \\ u_{\mathrm{C}}^{k+1} \end{bmatrix}, g^k\right). \end{aligned} \tag{36}$$

By analogy with the iterative equation of the backward Euler method [see (35)], the iterative equation for the trapezoidal Euler method can be obtained. Specifically, Δt in (35) is replaced with $\frac{\Delta t}{2}$, and $\begin{bmatrix} i_{\mathrm{L}}^k \\ u_{\mathrm{C}}^k \end{bmatrix}$ is replaced with $\begin{bmatrix} i_{\mathrm{L}}^k \\ u_{\mathrm{C}}^k \end{bmatrix} + \frac{\Delta t}{2} \cdot f(\begin{bmatrix} i_{\mathrm{L}}^k \\ u_{\mathrm{C}}^k \end{bmatrix}, g^k)$. The iterative equation for the trapezoidal Euler method is given by

$$\begin{bmatrix} i_{\mathrm{L}}^{k+1} \\ u_{\mathrm{C}}^{k+1} \end{bmatrix} = \begin{bmatrix} \rho|_{\mathrm{g}=0} \\ \bar{\rho}|_{\mathrm{g}=0} \end{bmatrix}^T \cdot \begin{bmatrix} \left(I - \frac{\Delta t}{2} \cdot A|_1\right)^{-1} \begin{bmatrix} i_{\mathrm{L}}^k \\ u_{\mathrm{C}}^k \end{bmatrix}^r \\ \left(I - \frac{\Delta t}{2} \cdot A|_0\right)^{-1} \begin{bmatrix} i_{\mathrm{L}}^k \\ u_{\mathrm{C}}^k \end{bmatrix}_0 \end{bmatrix} \cdot \left(1 - g^k\right)$$

$$+\begin{bmatrix}\rho|_{g=1}\\ \bar{\rho}|_{g=1}\end{bmatrix}^T\cdot\begin{bmatrix}\left(I-\frac{\Delta t}{2}\cdot A|_1\right)^{-1}\left(E\frac{\Delta t}{2}\cdot B|_1+\begin{bmatrix}i_{\mathrm{L}}^k\\ u_{\mathrm{C}}^k\end{bmatrix}_1^r\right)\\ \left(I-\frac{\Delta t}{2}\cdot A|_0\right)^{-1}\left(E\frac{\Delta t}{2}\cdot B|_0+\begin{bmatrix}i_{\mathrm{L}}^k\\ u_{\mathrm{C}}^k\end{bmatrix}_1^r\right)\end{bmatrix}\cdot g^k \tag{37}$$

where

$$\begin{bmatrix}i_{\mathrm{L}}^k\\ u_{\mathrm{C}}^k\end{bmatrix}_1^r=\begin{bmatrix}i_{\mathrm{L}}^k\\ u_{\mathrm{C}}^k\end{bmatrix}+\frac{\Delta t}{2}\cdot f\left(\begin{bmatrix}i_{\mathrm{L}}^k\\ u_{\mathrm{C}}^k\end{bmatrix},1\right)$$

$$\begin{bmatrix}i_{\mathrm{L}}^k\\ u_{\mathrm{C}}^k\end{bmatrix}_0^r=\begin{bmatrix}i_{\mathrm{L}}^k\\ u_{\mathrm{C}}^k\end{bmatrix}+\frac{\Delta t}{2}\cdot f\left(\begin{bmatrix}i_{\mathrm{L}}^k\\ u_{\mathrm{C}}^k\end{bmatrix},0\right)$$

$$\rho|_{g=1}=\left(\hat{i}_{\mathrm{L}}\big|_{g=1}>0\right)\vee\left(E>\hat{u}_{\mathrm{C}}|_{g=1}\right)$$

$$\rho|_{g=0}=\left(\hat{i}_{\mathrm{L}}|_{g=0}>0\right)\vee\left(0>\hat{u}_{\mathrm{C}}|_{g=0}\right)$$

$$\begin{bmatrix}\hat{i}_{\mathrm{L}}|_{g=1}\\ \hat{u}_{\mathrm{C}}|_{g=1}\end{bmatrix}=\left(I-\frac{\Delta t}{2}\cdot A|_1\right)^{-1}\left(E\frac{\Delta t}{2}\cdot B|_1+\begin{bmatrix}i_{\mathrm{L}}^k\\ u_{\mathrm{C}}^k\end{bmatrix}_1^r\right)$$

$$\begin{bmatrix}\hat{i}_{\mathrm{L}}|_{g=0}\\ \hat{u}_{\mathrm{C}}|_{g=0}\end{bmatrix}=\left(I-\frac{\Delta t}{2}\cdot A|_1\right)^{-1}\begin{bmatrix}i_{\mathrm{L}}^k\\ u_{\mathrm{C}}^k\end{bmatrix}_0^r.$$

E. Numerical Boundary Handling

The proposed model involves equality logic judgments, i.e., $i_{\mathrm{L}}=0$. It should be noted that although the model only contains the logical expression $i_{\mathrm{L}}>0$ and does not explicitly include $i_{\mathrm{L}}=0$, this is because the latter is eliminated during logical simplification. In other words, when $i_{\mathrm{L}}>0$ does not hold, it implies $i_{\mathrm{L}}=0$.

When the true value of i_{L} is zero, numerical solutions may lie within a neighborhood around zero, i.e., $\xi_-<0<\xi_+$. Consequently, strict equality cannot be enforced in numerical computation, necessitating the definition of judgment boundaries. In the proposed model, the condition $i_{\mathrm{L}}>0$ is, therefore, implemented as $i_{\mathrm{L}}>\xi_+$, where ξ_+ is a small positive threshold, such as 10^{-6}.

The same approach is applied when handling equality logic judgments in expressions, such as $E\leqslant u_{\mathrm{C}}$ or $u_{\mathrm{C}}\geqslant 0$. Specifically, $E>u_{\mathrm{C}}$ is treated as $E-u_{\mathrm{C}}>\xi_+$, and $u_{\mathrm{C}}<0$ is treated as $u_{\mathrm{C}}<\xi_-$.

In addition, it should be noted that in this article, the equality condition is assigned to the cases of $E<u_{\mathrm{C}}$ and $u_{\mathrm{C}}>0$. Alternatively, it could also be assigned to $E>u_{\mathrm{C}}$ and $u_{\mathrm{C}}<0$. The procedure for handling equality logic judgments remains the same, and is, therefore, not reiterated here.

V. Application of the Proposed Model in Model-Based Control Methods

The proposed models only include a few additional logical variables without requiring piecewise functions or inequality constraints, making them closely aligned with the CCM models. These models retain the form of a nonlinear state-space equation $\dot{\boldsymbol{x}}=f(\boldsymbol{x},\boldsymbol{u})$, thereby enabling straightforward integration with existing CCM model-based control methods, such as MPC.

Next, we illustrate how to integrate the proposed model into the existing MPC using a buck converter as an example.

1) *Decision variables:* The decision variables are the control inputs from time t to $t+(N-1)\Delta t$, and the inductor current and capacitor voltage from $t+\Delta t$ to $t+N\Delta t$

$$u^0,i_{\mathrm{L}}^1,u_{\mathrm{C}}^1,\ldots,u^{N-1},i_{\mathrm{L}}^N,u_{\mathrm{C}}^N$$

where i_L^k and u_C^k denote $i_L(t+k\Delta t)$ and $u_C(t+k\Delta t)$, respectively. If the switch signal g is the control input, then u^k is $g(t+k\Delta t)$; if the duty cycle d is the control input, then u^k is $d(t+k\Delta t)$.

2) *Objective function:* The control objective is to maintain the capacitor voltage u_{C} at a reference value $u_{\mathrm{C}}^{\mathrm{ref}}$. The optimization goal is defined as

$$\min J=w_1\sum_{k=1}^{N}\left(u_{\mathrm{C}}^k-u_{\mathrm{C}}^{\mathrm{ref}}\right)^2+w_2\sum_{k=1}^{N}\left(i_{\mathrm{L}}^k-i_{\mathrm{L}}^{\mathrm{ref}}\right)^2$$

where the reference inductor current $i_{\mathrm{L}}^{\mathrm{ref}}$ is given by $\frac{u_{\mathrm{C}}^{\mathrm{ref}}}{R}$, while w_1 and w_2 serve as the weighting coefficients.

3) *Constraints:* The constraints consist of the range of the duty cycle and the equality constraints imposed by the state-space equation. These equality constraints can be represented by the discrete forms, as shown in (23), (25), (35), and (36). Considering the tradeoff between computational effort and accuracy, the Euler method is most commonly used, whereas the other three solvers, although more accurate, are less practical for real-time MPC. Therefore, we select (23) to construct the equality constraints:

$$\begin{cases}\frac{L}{\Delta t}\left(i_{\mathrm{L}}^{k+1}-i_{\mathrm{L}}^k\right)=\eta_1^k\left(E-u_{\mathrm{C}}^k\right)u^k-\eta_2^k u_{\mathrm{C}}^k\left(1-u^k\right)\\ \frac{C}{\Delta t}\left(u_{\mathrm{C}}^{k+1}-u_{\mathrm{C}}^k\right)=i_{\mathrm{L}}^k-\frac{u_{\mathrm{C}}^k}{R}\\ 0\leqslant u^k\leqslant 1 \text{ or } u^k\in\{0,1\}\end{cases}$$

where for duty cycle input, the constraint is $0\leqslant u^k\leqslant 1$, and for switch signal input, it is $u^k\in\{0,1\}$; $\eta_1^k=(i_{\mathrm{L}}^k>0)\vee(E>u_{\mathrm{C}}^k)$ and $\eta_2^k=(i_{\mathrm{L}}^k>0)\vee(u_{\mathrm{C}}^k<0)$.

Compared to the CCM model-based MPC, the proposed model-based MPC includes state descriptors only in the constraints without altering the overall structure of the control scheme. Therefore, the proposed model maintains compatibility with existing control methods while providing improved accuracy in predicting system behavior.

VI. Case Study

A. Model Accuracy Verification

We constructed dc–dc converters in MATLAB/Simulink as benchmarks and employed the fourth-order Runge–Kutta method to solve the proposed models. The accuracy of the models was verified by comparing the numerical solutions with the results obtained from Simulink. Due to the large number of converters involved, this section focuses on a detailed case study of the buck converter, boost converter, and buck–boost converter, with additional case studies for other converters provided in Appendix B. Buck converter's parameters: $L=2$ mH, $C=0.5$ mF, $V_{\mathrm{in}}=400$ V, $V_{\mathrm{out}}=300$ V, $f_c=10$ kHz, and $d=0.75$. Boost con-

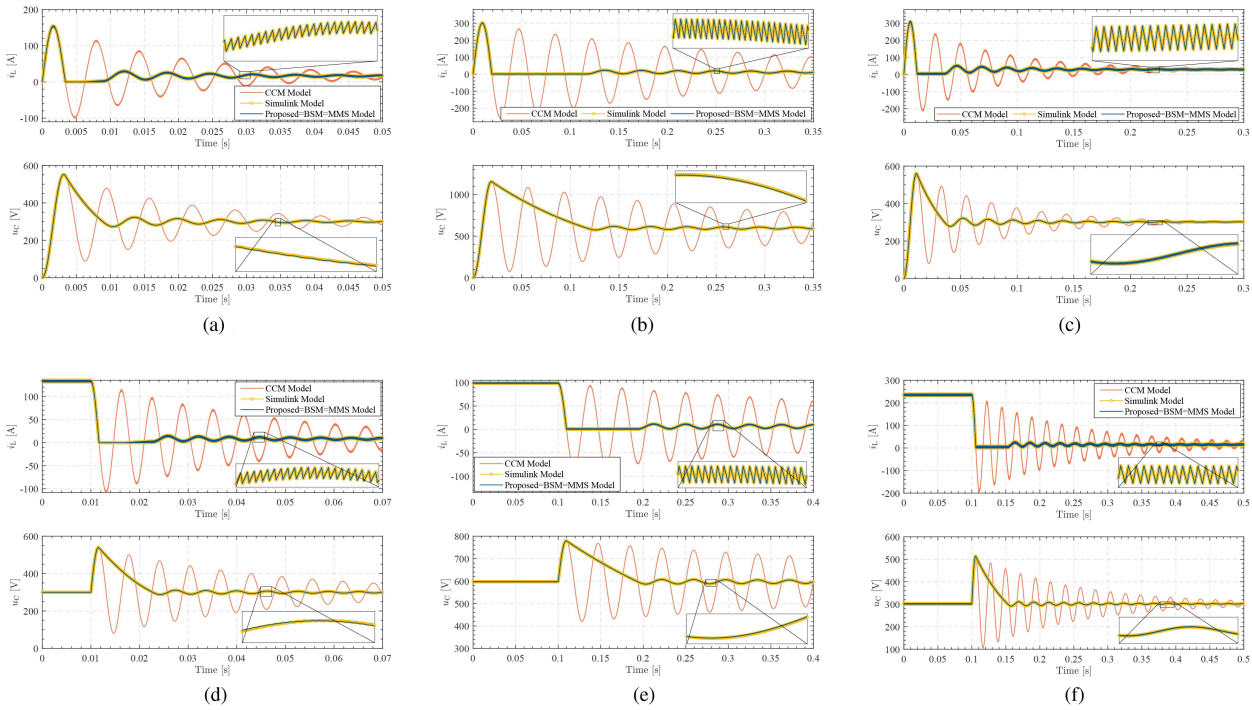

Fig. 11. Outcomes of CCM, hybrid, and proposed models. (a) Scenario 1 + Buck converter. (b) Scenario 1 + Boost converter. (c) Scenario 1 + Buck–boost converter. (d) Scenario 2 + Buck converter. (e) Scenario 2 + Boost converter. (f) Scenario 2 + Buck–boost converter.

TABLE II
COMPARISON OF MODEL ACCURACY WITH R^2 METRIC

Scenario	Model	R^2	Buck	Boost	Buck–boost
1	CCM	i_L	−1.4493	−5.5932	−1.3911
		u_C	−0.7332	−1.8644	−0.6443
	Proposed =BSM=MMS	i_L	0.9999	0.9999	0.9999
		u_C	0.9999	0.9999	0.9999
2	CCM	i_L	0.0942	−0.0168	0.6190
		u_C	−2.5364	−3.2397	−2.1557
	Proposed =BSM=MMS	i_L	0.9999	0.9999	0.9999
		u_C	0.9999	0.9999	0.9999

TABLE III
COMPARISON OF MODEL ACCURACY WITH MSE METRIC

Scenario	Model	MSE	Buck	Boost	Buck-Boost
1	CCM	i_L	1535.51	14866.69	1475.32
		u_C	7812.92	82757.12	7412.11
	Proposed =BSM=MMS	i_L	0.0023	0.0009	0.0020
		u_C	0.0095	0.0068	0.0086
2	CCM	i_L	1889.54	1746.86	1248.97
		u_C	9917.54	9095.71	8503.25
	Proposed =BSM=MMS	i_L	0.0233	0.0018	0.0019
		u_C	0.1640	0.0078	0.0009

verter's parameters: $L = 8$ mH, $C = 2$ mF, $V_{\text{in}} = 400$ V, $V_{\text{out}} = 600$V, $f_c = 10$ kHz, and $d = 0.33$. Buck–boost converter's parameters: $L = 2$ mH, C=2 mF, $V_{\text{in}} = 400$ V, $V_{\text{out}} = 300$ V, $f_c = 10$ kHz, $d = 0.4286$. Two test scenarios were considered as follows:

1) *Scenario 1:* Startup with a 5 kW load.
2) *Scenario 2:* The converters initially operates with a 40-kW load, and subsequently, a 37.5-kW load is removed.

The comparison test encompasses the CCM models, the BSM models from [32], the MMS models from [33], and the proposed models. The models were solved using the fourth-order Runge–Kutta method with a time step of 1 μs and the Simulink models used the ODE4 solver with the same time step. The accuracy metrics were the coefficient of determination $R^2 \in (-\infty, 1]$ and the mean squared error (mse $\in [0, +\infty)$). A value of R^2 closer to 1 indicates higher model accuracy, while an mse closer to 0 is better. The results are presented in Tables II, III, and Fig. 11.

As evident from Table II and Fig. 11, there is a significant discrepancy between the CCM model and the Simulink results, particularly in the solution after current discontinuity. The CCM model assumes that switches and diodes are always conductive, leading to negative current values when facing discontinuous current conditions. Thus, the CCM model's low accuracy is mainly due to its failure to include the cutoff states of switches and diodes.

As shown in Table II, both the proposed models and the BSM models and the MMS models achieve a near-perfect match with the physical models, boasting a fitting rate of 99.99% for both inductor current and capacitor voltage. Fig. 11 further illustrates that these models can precisely predict system behavior, even achieving an almost perfect fit for the ripples. While both sets of models demonstrate exceptional precision, the proposed models stand out for its conciseness, requiring only 1 and 2 logical variables to achieve what the BSM models and the MMS models need multiple logical variables and inequalities to accomplish.

In summary, the proposed models add only 1 and 2 logical variables to the CCM models, yet it achieves results comparable to the Simulink models. They surpass the CCM models in accuracy and the hybrid models in complexity.

TABLE IV
MPC COMPUTATIONAL TIME: BUCK CONVERTER

XXX-based MPC	Index	Computational time for different prediction lengths [μs]							
		1	2	3	4	5	6	7	8
CCM model	Total	5.98	8.04	11.79	19.84	34.01	70.26	106.17	216.44
	Logical	-	-	-	-	-	-	-	-
	Arithmetic	1.45	2.65	4.43	7.34	14.40	24.93	46.12	94.28
Proposed model	Total	7.05	10.29	15.45	26.13	43.63	86.20	133.16	244.89
	Part I	1.59	2.79	4.31	6.36	10.74	16.34	28.07	51.02
	Part II	1.65	3.06	5.07	8.55	15.92	28.49	52.79	106.57
BSM model	Total	10.51	17.34	27.33	43.01	68.78	134.98	214.76	410.58
	Logical	4.15	8.03	12.62	19.34	32.43	53.28	88.63	176.62
	Arithmetic	2.59	4.84	8.84	12.85	23.33	39.41	72.01	134.88

B. Controller Performance Verification

1) Case Study: Buck Converter: To demonstrate the superiority of the proposed model in model-based control methods, we applied the CCM model, the BSM model, and the proposed model to the MPC method presented in [11]. The parameters of the buck converter are: $L = 2$ mH, $C = 3$ mF, input voltage $=$ 400 V, and output voltage $=$ 300 V. The case studies were conducted from two perspectives: computational time and control performance.

Part I: Computational time analysis: The MPC algorithm based on different models is implemented in C++. The *chrono* library in C++ is used to measure the computational time. Specifically, the *high_resolution_clock* function captures the start and end times of the algorithm execution. The duration is calculated using the *duration* class, providing the elapsed time in a specified unit (e.g., milliseconds). The Raspberry Pi 4B is used as the test platform. The algorithm is executed 5000 times, and the average running time is calculated.

We assessed three key aspects: 1) total computation time needed to generate control signals; 2) time for model logical operations, including calculating logical variables (η for the proposed model and δ for the BSM model) during predictions; and 3) time for model arithmetic operations during predictions. These times are detailed in Table IV.

According to Table IV, in terms of logical operations, the proposed model enhances efficiency by 66.95% compared to the BSM model. The BSM model is significantly more complex than the proposed model when calculating logical variables. The BSM model involves complex quadratic polynomial operations and requires logical judgments, whereas the proposed model only requires computing two logical expressions. Regarding arithmetic operations, the proposed model improves performance by 32.04% over the BSM model. The BSM model involves three operations (matrix subtraction, multiplication with logical variables, and matrix addition). In contrast, the proposed model is simpler, involving only the multiplication of logical variables with scalars. In terms of overall computation time, the BSM model-based MPC requires 2.03 times the computation time of the CCM model-based MPC, while the proposed model-based MPC only needs 1.25 times. This gives the proposed model a distinct advantage in long-term optimization control scenarios. For instance, when the prediction length is 7, the BSM model-based MPC takes 214 μs, whereas the proposed model-based MPC requires only 133 μs.

In conclusion, the proposed model, when applied to model predictive control, significantly reduces computational complexity and improves computational efficiency.

Part II: Proposed model-based MPC versus BSM model-based MPC: To verify the improvement in control performance due to the enhanced computational efficiency, a comparative analysis is conducted between the proposed model-based MPC and the BSM model-based MPC. The test scenario consists of a load power that initially starts at 20 kW, then changes to 80 kW, and finally returns to 20 kW. The prediction horizons N are varied from 5 to 8. The control cycles of the proposed model-based MPC and the BSM model-based MPC are set based on the prediction horizons and Table IV. For $N = 5$ to $N = 8$, the control cycles for the proposed model-based MPC were 100, 100, 150, and 250 μs, respectively, while those for the MMS model-based MPC were 100, 150, 250, and 400 μs. The results are illustrated in Fig. 12.

As shown in Fig. 12, both the proposed and BSM model-based MPCs can compute within 150 μs for $N = 5$ and $N = 6$, showing similar performance. However, for $N = 7$, the BSM model-based MPC, due to its higher computational load, requires a 250-microsecond control cycle, while the proposed model-based MPC only needs 150 μs. This allows the proposed model-based MPC to respond promptly to voltage changes, achieving better steady-state control and transient response. When $N = 8$, the BSM model-based MPC's substantial computational demands lead to significant steady-state voltage fluctuations, which can be regarded as a control failure. In contrast, the proposed model-based MPC continues to provide effective control in both transient and steady-state conditions.

In summary, the proposed model-based MPC achieves higher computational efficiency than the BSM model-based MPC, thereby enabling faster voltage response and consequently enhancing voltage control performance.

Part III: Proposed model-based MPC versus CCM model-based MPC: To evaluate the impact of model accuracy on model-based control algorithms, the proposed model-based MPC is compared with the CCM model-based MPC. The load power starts at 50 kW and then decreases to 2.5 kW. The condition leads to discontinuous inductor current, thereby highlighting the

TABLE V
MPC COMPUTATIONAL TIME: BOOST CONVERTER

XXX-based MPC	Index	Computational time for different prediction lengths [μs]							
		1	2	3	4	5	6	7	8
CCM model	Total	5.93	7.84	11.68	19.50	34.63	76.11	99.42	216.77
	Logical	-	-	-	-	-	-	-	-
	Arithmetic	1.51	2.74	4.34	7.36	13.43	27.35	44.20	89.38
Proposed model	Total	6.67	10.25	15.59	26.98	40.90	86.19	129.41	245.67
	Part I	1.56	2.70	4.25	6.25	9.98	15.10	28.63	47.39
	Part II	1.61	3.05	5.15	9.17	15.89	30.70	51.85	110.64
MMS model	Total	10.36	17.23	22.72	41.23	63.52	121.29	209.39	397.28
	Logical	3.63	6.98	10.24	16.31	27.73	44.77	81.08	159.77
	Arithmetic	2.44	4.9	8.76	12.39	22.07	38.22	70.22	126.65

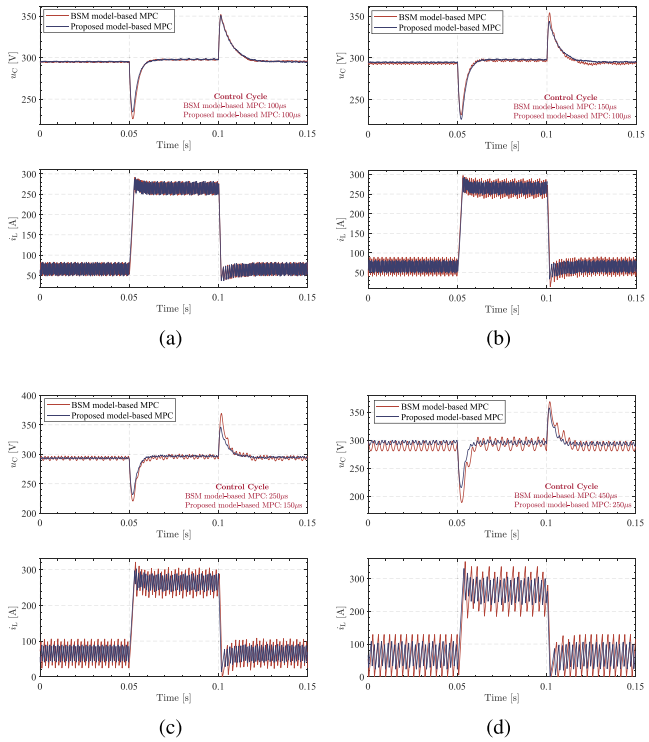

Fig. 12. Comparative results of proposed and BSM model-based MPC for buck converter. (a) $N = 5$. (b) $N = 6$. (c) $N = 7$. (d) $N = 8$.

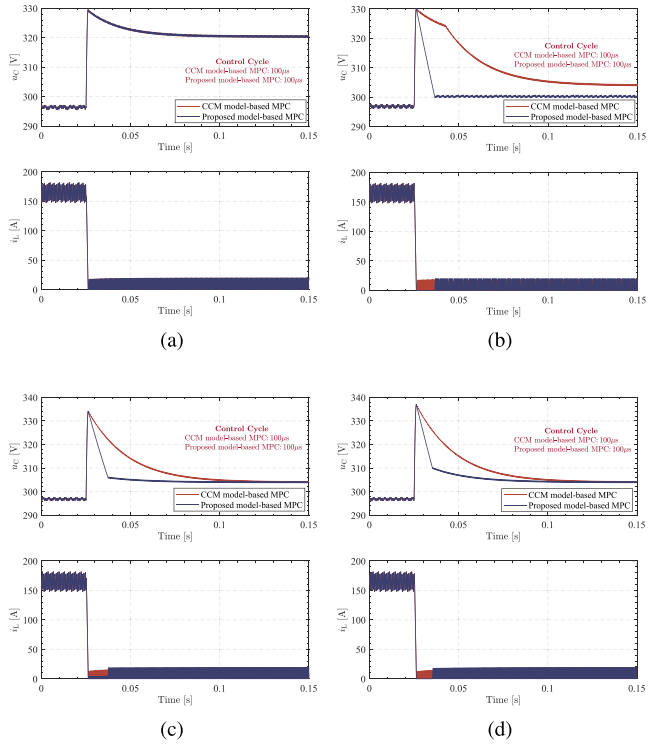

Fig. 13. Comparative results of proposed and CCM model-based MPC for buck converter. (a) $N = 3$. (b) $N = 4$. (c) $N = 5$. (d) $N = 6$.

differences between the models. The prediction length is varied from 3 to 6. Since both the proposed and hybrid model-based MPCs can complete computations within 100 μs, the control cycle is set to 100 μs. The results are presented in Fig. 13.

As shown in Fig. 13, compared to the CCM model-based MPC, the hybrid model-based MPC achieves a 35.69% reduction in voltage response time. When the prediction length $N = 3$, neither the proposed model-based MPC nor the CCM model-based MPC can achieve effective control following the disturbance. For prediction lengths of $N = 4$, $N = 5$, and $N = 6$, both MPCs ultimately stabilize the voltage around 300 V. Nevertheless, the proposed model-based MPC exhibits markedly superior control performance, characterized by a more rapid response and substantially lower cumulative voltage error in comparison to the CCM model-based MPC. This enhanced performance can be attributed to the accurate prediction of inductor current during discontinuities by the proposed model. In contrast, the CCM model inaccurately forecasts the inductor current during these periods, leading the CCM model-based MPC to continue charging the inductor. This action is erroneous, as the optimal solution during current discontinuities—when the voltage exceeds the reference value—is to deactivate the switch and thereby interrupt the energy supply from the source.

In summary, the proposed model exhibits significantly higher accuracy compared to the CCM model. This enhanced accuracy translates into superior performance for model-based control methods.

2) Case Study: Boost Converter: We conducted case studies using a boost converter, comparing the proposed model with the CCM model and the MMS model. The boost converter parameters are as follows: $L = 2$ mH, $C = 3$ mF, input volt-

age = 200 V, and output voltage = 500 V. The case studies were conducted from two perspectives: computational time and control performance.

Part I: Computational time analysis: The total computation time and the time consumed by logical operations and arithmetic operations are presented in Table V. In terms of logical operations, the proposed model achieves a 62.90% improvement in computational efficiency compared to the hybrid model. Regarding arithmetic operations, the proposed model improves efficiency by 28.16%. These improvements are slightly lower than those observed in the buck converter tests (66.95% and 32.04%, respectively), as the MMS model further simplifies variables and constraints compared to the BSM model. In terms of overall computation time, the MMS model requires 1.918 times the computation time of the CCM model, while the proposed model requires only 1.236 times. Considering both total computation time and the time consumed by logical and arithmetic operations, the proposed model once again demonstrates its low complexity and its advantages in improving computational efficiency when applied in MPC.

Part II: Proposed model-based MPC versus MMS model-based MPC: Using the Boost converter as an example, we compared the performance of MPC based on the proposed model and the MMS model. The test scenario involved a load power that initially started at 50 kW, then changed to 20 kW, and finally returned to 50 kW. The prediction horizon N varied from 5 to 8. The control cycles for both MPCs were set based on the prediction horizon and Table V. For $N = 5$ to $N = 8$, the control cycles for the proposed model-based MPC were 100, 100, 150, and 250μs, respectively, while those for the MMS model-based MPC were 100, 150, 250, and 400μs. The results are illustrated in Fig. 14.

As shown in Fig. 14, when $N = 5$, both MPCs based on the proposed model and the MMS model complete the computation within 100 μs, resulting in similar performance. When $N = 6$, the proposed model-based MPC only reduces the control cycle by 50 μs compared to the MMS model, showing minimal performance difference. However, when $N = 7$ and $N = 8$, the difference in control cycles becomes significant. The MMS model-based MPC, with its longer control cycle, exhibits larger ripples and greater voltage fluctuations. Particularly at $N = 8$, the MMS model-based MPC shows noticeable steady-state voltage deviation. In contrast, the proposed model-based MPC demonstrates faster dynamic voltage response and smaller steady-state deviation for $N = 7$ and $N = 8$, further highlighting the superiority of the proposed model in control applications.

Part III: Proposed model-based MPC versus CCM model-based MPC: We compared the MPC performance using the proposed and hybrid models. The test scenario includes a load power starting at 50 kW, dropping to 20 kW, and returning to 50 kW. The prediction horizon N ranges from 4 to 7. Both MPCs complete computations within 100 μs, so the control cycle is set to 100 μs. Results are shown in Fig. 15.

Fig. 15 shows that for $N = 4$ and $N = 5$, neither MPC can maintain the voltage at 500 V following a load disturbance. At $N = 6$, the CCM model-based MPC still cannot

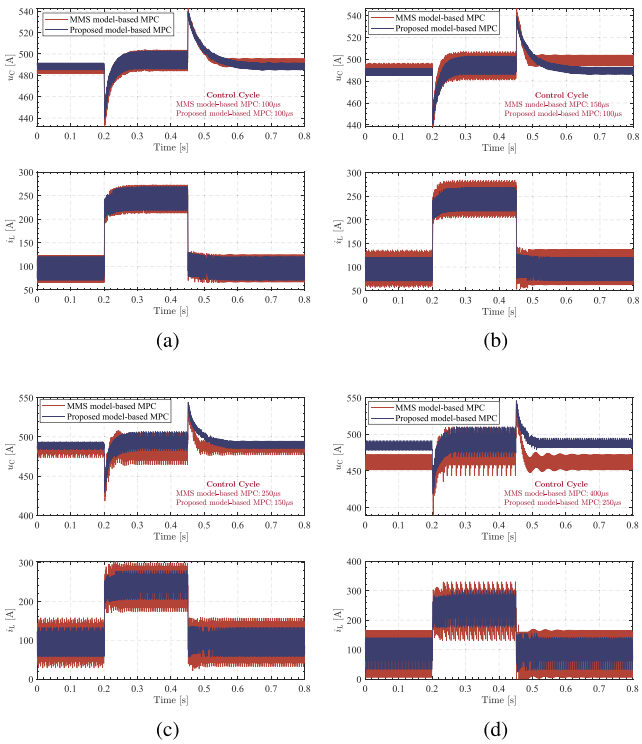

Fig. 14. Comparative results of proposed and MMS model-based MPC for boost converter. (a) $N = 5$. (b) $N = 6$. (c) $N = 7$. (d) $N = 8$.

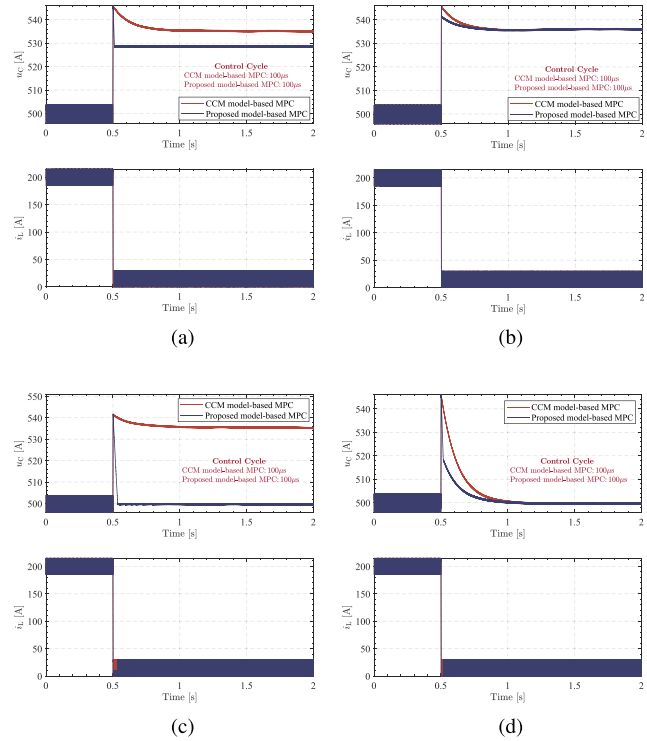

Fig. 15. Comparative results of the proposed and CCM model-based MPC for boost converter. (a) $N = 5$. (b) $N = 6$. (c) $N = 7$. (d) $N = 8$.

TABLE VI
RESULTS UNDER DIFFERENT NUMERICAL SOLUTION METHODS

Index	Forward Euler		Runge-Kutta	
	i_L	u_C	i_L	u_C
R^2	0.9999	0.9997	0.9999	0.9999
MES	0.1232	0.9118	0.0233	0.1640
Index	Backward Euler		Trapezoidal Euler	
	i_L	u_C	i_L	u_C
R^2	0.9999	0.9999	0.9999	0.9999
MSE	0.0238	0.1094	0.0234	0.1640

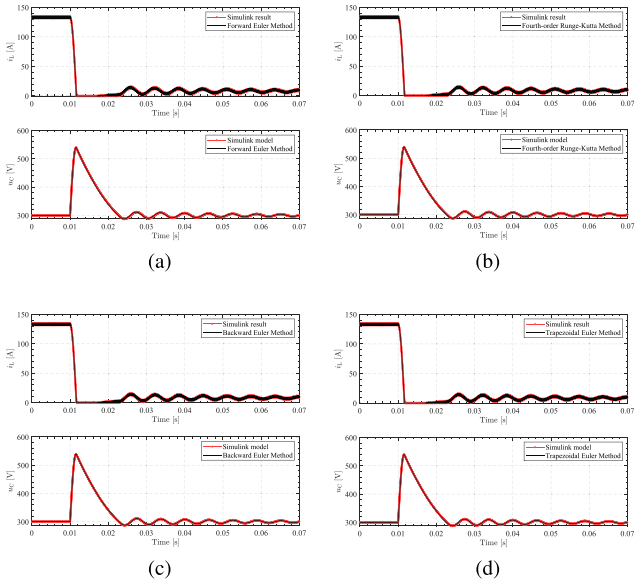

Fig. 16. Results under different numerical solvers. (a) Forward Euler method. (b) Fourth-order Runge–Kutta method. (c) Backward Euler method. (d) Trapezoidal Euler method.

control the voltage to 500 V, whereas the proposed model-based MPC can rapidly stabilize the voltage at 500 V. When $N = 7$, although both MPCs can maintain the voltage at 500 V, the proposed model-based MPC exhibits faster voltage recovery and smaller dynamic deviation. This advantage stems from the proposed model's accurate identification of whether the circuit is in DCM or CCM, enabling more precise decision-making when the converter enters DCM. These findings underscore the significant benefits of accurately distinguishing between DCM and CCM for enhanced control performance.

C. Analysis on Numerical Solving

We compared the results obtained from the forward Euler method, the fourth-order Runge–Kutta method, the backward Euler method, and the Trapezoidal Euler method with those from a Simulink model. The time step used was 1 μs, and the Simulink solver employed was ode4. The conditions were as follows: The buck converter initially operated with a 40-kW load, which was subsequently reduced to 37.5 kW. The results of the four methods are presented in Table VI and Fig. 16.

As shown in Table VI, the R^2 values for all four numerical solvers are extremely high, approaching 1, indicating that these

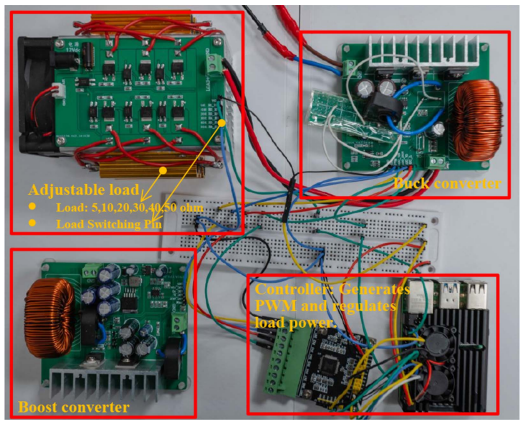

Fig. 17. Hardware experiment platform.

TABLE VII
PARAMETERS OF BUCK AND BOOST CONVERTER PROTOTYPES

Converter	ΔV_S	R_S	ΔV_D	R_D
Buck	0.038V	0.042Ω	0.190V	0.269Ω
Boost	0.143V	0.094Ω	0.061V	0.151Ω
Converter	L	R_L	C	R_C
Buck	2.91mH	0.003Ω	0.44mF	0.100Ω
Boost	1.63mH	0.099Ω	1.56mF	0.095Ω

methods closely match the Simulink results with a high degree of accuracy. The waveforms, as depicted in Fig. 16, demonstrate that the output from each of the four methods aligns well with the Simulink model's output in both detail and overall trend.

In summary, the proposed model is fully compatible with classical numerical solution methods, and the state descriptor η in the proposed model does not influence the choice of solver.

D. Hardware Experiment

To verify the accuracy of the proposed model, we conducted hardware experiments on the buck and boost converters, as shown in Fig. 17. The duty cycle was set to 0.5, and the pulsewidth modulation frequency was 100 kHz. The experiments were divided into the following six cases:

1) Buck converter: input voltage E_1, initial load as parallel combination of R_{50} and R_5, then R_5 removed.
2) Buck converter: input voltage E_1, initial load as parallel combination of R_{40} and R_5, then R_5 removed.
3) Buck converter: input voltage E_1, initial load as parallel combination of R_{30} and R_5, then R_5 removed.
4) Boost converter: input voltage E_2, initial load as parallel combination of R_{50} and R_5, then R_5 removed.
5) Boost converter: input voltage E_2, initial load as parallel combination of R_{40} and R_5, then R_5 removed.
6) Boost converter: input voltage E_2, initial load as parallel combination of R_{30} and R_5, then R_5 removed.

where $E_1 = 19.66$ V, $E_2 = 10.33$V, $R_{50} = 53.42\,\Omega$, $R_{40} = 43.38\Omega$, $R_{30} = 31.86\Omega$, $R_5 = 5.52\Omega$.

The parameters of the buck and boost converters were obtained using a parameter identification algorithm, as shown in

TABLE VIII
EVALUATION OF THE PROPOSED MODEL'S ACCURACY USING EXPERIMENTAL AND SIMULINK RESULTS

Benchmark	MSE	Case 1	Case 2	Case 3	Case 4	Case 5	Case 6
Simulink	i_{L}	0.0777×10^{-5}	0.7298×10^{-5}	0.6995×10^{-5}	0.2220×10^{-5}	0.2063×10^{-5}	0.2031×10^{-5}
	u_{C}	0.1604×10^{-5}	0.8594×10^{-5}	0.3281×10^{-5}	0.0185×10^{-5}	0.0172×10^{-5}	0.0176×10^{-5}
Experiment	i_{L}	0.0019	0.0013	0.0018	0.0110	0.0136	0.0168
	u_{C}	0.0062	0.0022	0.0031	0.0331	0.0627	0.0622
Benchmark	R^2	Case 1	Case 2	Case 3	Case 4	Case 5	Case 6
Simulink	i_{L}	0.9999	0.9999	0.9999	0.9999	0.9999	0.9999
	u_{C}	0.9999	0.9999	0.9999	0.9999	0.9999	0.9999
Experiment	i_{L}	0.9972	0.9968	0.9970	0.9984	0.9985	0.9981
	u_{C}	0.9800	0.9804	0.9864	0.9870	0.9802	0.9788

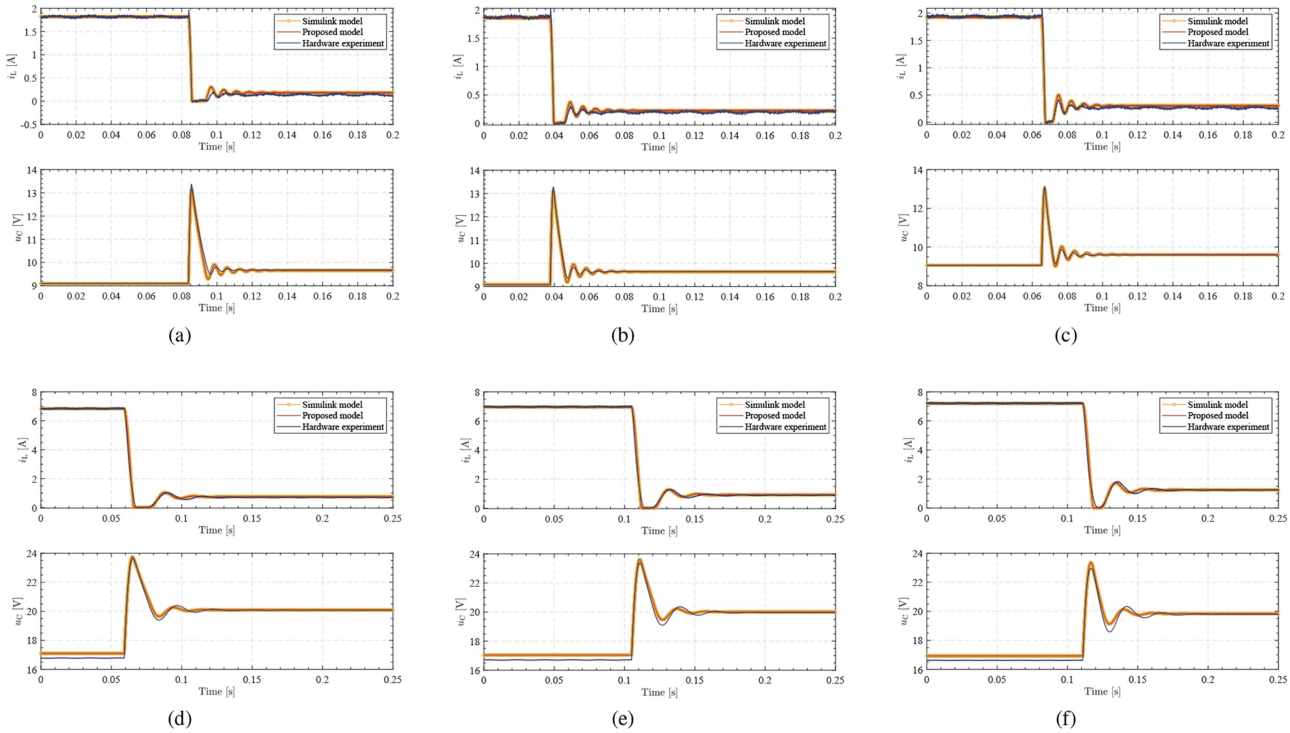

Fig. 18. Comparison of experimental results, simulink simulation results, and proposed model results. (a) Case1. (b) Case2. (c) Case3. (d) Case4. (e) Case5. (f) Case6.

Table VII. The proposed model was configured according to Table VII and the six conditions, and then solved using the Fourth-order Runge–Kutta method to obtain the model results. Taking the oscilloscope waveform data as the benchmark, the model results and Simulink results were evaluated using R^2 and mse, with the results shown in Table VIII. The Simulink results, model results, and oscilloscope waveform data were plotted on the same graph, as shown in Fig. 18.

Table VIII shows that the proposed model matches the Simulink model perfectly and achieves a fitting rate of over 97% with the experimental results, thereby verifying its accuracy. As depicted in Fig. 18, the proposed model's results align well with the experimental data. Regarding steady-state performance, the proposed buck converter model exhibits negligible steady-state error, while the boost converter model shows a slight deviation before power disturbances but none afterward. In terms of transient performance, the proposed model closely matches the experimental results in terms of oscillation amplitude and count, as well as the timing and duration of current discontinuities.

In summary, the proposed model, which incorporates nonideal factors, closely aligns with the experimental results and effectively captures the steady-state and transient dynamics observed in physical experiments, whether the current is continuous or discontinuous.

VII. CONCLUSION

With the widespread application of dc–dc converters in high power quality scenarios, their transient performance has received unprecedented attention. Existing models struggle to support model-based control methods: CCM models fail to accurately describe converter behavior during switching between CCM and DCM, and hybrid models are overly complex, hindering their practical application. This article proposes a

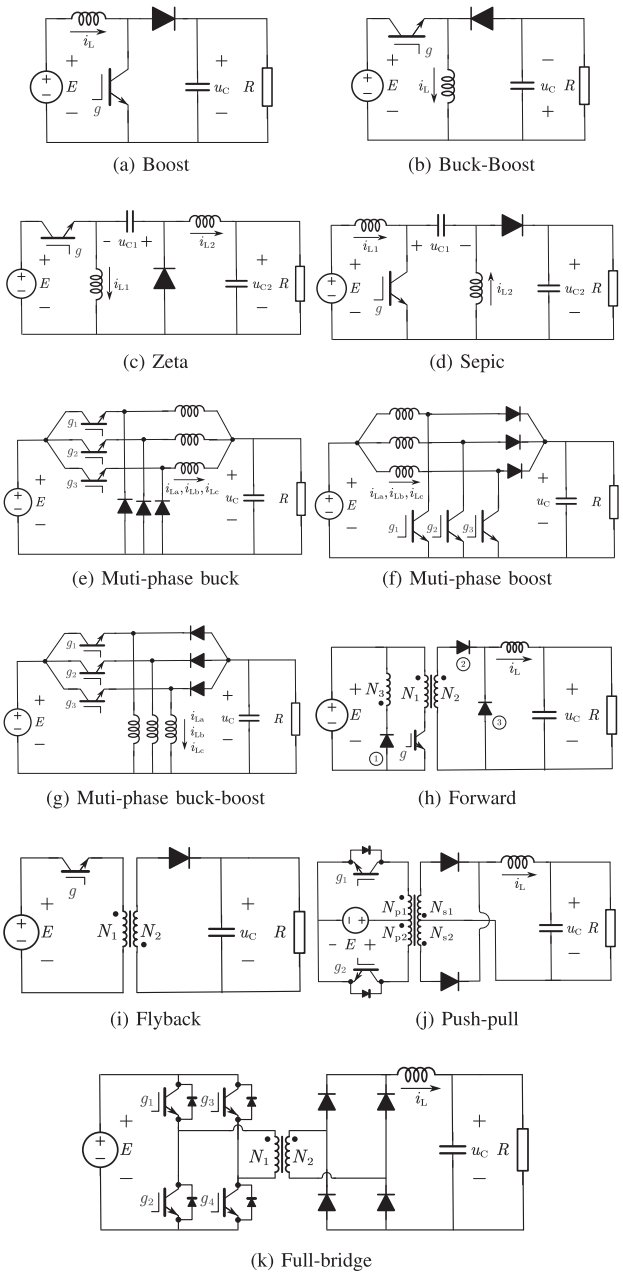

Fig. 19. Topologies of typical DC–DC converters. (a) Boost. (b) Buck–boost. (c) Zeta. (d) Sepic. (e) Multiphase buck. (f) Multiphase boost. (g) Multiphase buck–boost. (h) Forward. (i) Flyback. (j) Push–pull. (k) Full-bridge.

state quadrant modeling approach to establish a concise and high-precision models. The conclusions are as follows.

1) The proposed method offers both exceptional precision and excellent scalability. It is suitable for a variety of converters, including single-inductor, dual-inductor, multiphase, bidirectional, and isolated types, maintaining an accuracy rate of 99.99% across all these converter types.
2) The high precision of the proposed models enhances the performance of model-based control methods. Compared to the CCM model-based MPC, the proposed model-based MPC reduces the voltage response time by 35.69%.
3) The proposed models have concise mathematical forms and low computational complexity, making it easily applicable to model-based control methods. For instance, when applied in MPC, the proposed model reduces computational time by 36.85%.

APPENDIX

A. Topologies of DC–DC Converters

Figs. 4 and 7 illustrate the topologies of buck converters and cuk converters, respectively, while the topologies of the remaining converters are shown in Fig. 19.

B. Model Accuracy Verification for Remaining Converters

Section VI-A provides a detailed model accuracy verification for the buck converter, boost converter, and buck–boost converter. Case studies for the remaining converters are presented here. The test scenario involved a significant high-power load disturbance, with the load power being P_1 before 0.1 s and P_2 after 0.1 s. The waveforms are illustrated in Fig. 20. The parameters for the converters are as follows.

1) *Cuk converter:* $E = 200\,\text{V}$, $u_{\text{out}}^{\text{ref}} = 400\,\text{V}$, $d = 0.666$, $L_1 = 1 \times 10^{-3}\,\text{H}$, $L_2 = 1 \times 10^{-3}\,\text{H}$, $C_1 = 5 \times 10^{-3}\,\text{F}$, $C_2 = 5 \times 10^{-3}\,\text{F}$, $P_1 = 100\,\text{kW}$, and $P_2 = 20\,\text{kW}$.
2) *Zeta converter:* $E = 200\,\text{V}$, $u_{\text{out}}^{\text{ref}} = 400\,\text{V}$, $d = 0.666$, $L_1 = 1 \times 10^{-3}\,\text{H}$, $L_2 = 1 \times 10^{-3}\,\text{H}$, $C_1 = 5 \times 10^{-3}\,\text{F}$, $C_2 = 5 \times 10^{-3}\,\text{F}$, $P_1 = 100\,\text{kW}$, and $P_2 = 20\,\text{kW}$.
3) *Sepic converter:* $E = 200\,\text{V}$, $u_{\text{out}}^{\text{ref}} = 400\,\text{V}$, $d = 0.666$, $L_1 = 1 \times 10^{-3}\,\text{H}$, $L_2 = 1 \times 10^{-3}\,\text{H}$, $C_1 = 5 \times 10^{-3}\,\text{F}$, $C_2 = 5 \times 10^{-3}\,\text{F}$, $P_1 = 100\,\text{kW}$, and $P_2 = 20\,\text{kW}$.
4) *Forward converter:* $E = 200\,\text{V}$, $u_{\text{out}}^{\text{ref}} = 300\,\text{V}$, $N_1 = 100$, $N_2 = 200$, $N_3 = 10$, $d = 0.75$, $L_{\text{m}} = 2\,\text{H}$, $L = 2 \times 10^{-3}\,\text{H}$, $C = 2 \times 10^{-3}\,\text{F}$, $P_1 = 40\,\text{kW}$, and $P_2 = 2.5\,\text{kW}$.
5) *Flyback converter:* $E = 400\,\text{V}$, $u_{\text{out}}^{\text{ref}} = 600\,\text{V}$, $N_1 = 100$, $N_2 = 200$, $d = 0.4286$, $L_{\text{m}} = 2 \times 10^{-3}\,\text{H}$, $C = 2 \times 10^{-3}\,\text{F}$, $P_1 = 100\,\text{kW}$, and $P_2 = 10\,\text{kW}$.
6) *Push–pull converter:* $E = 200\,\text{V}$, $u_{\text{out}}^{\text{ref}} = 300\,\text{V}$, $N_1 = 100$, $N_2 = 200$, $L_{\text{m}} = 5\,\text{H}$, $R = 1 \times 10^{6}\,\Omega$, $d = 0.625$, $L = 2 \times 10^{-3}\,\text{H}$, $C = 2 \times 10^{-3}\,\text{F}$, $P_1 = 100\,\text{kW}$, and $P_2 = 10\,\text{kW}$.
7) *Full-bridge converter:* $E = 200\,\text{V}$, $u_{\text{out}}^{\text{ref}} = 400\,\text{V}$, $N_1 = 100$, $N_2 = 300$, $L_{\text{m}} = 5\,\text{H}$, $R = 1 \times 10^{6}\,\Omega$, $\theta = 120^{\circ}$, $L = 2 \times 10^{-3}\,\text{H}$, $C = 2 \times 10^{-3}\,\text{F}$, $P_1 = 100\,\text{kW}$, and $P_2 = 10\,\text{kW}$.
8) *Multiphase Buck–boost converter:* $E = 400\,\text{V}$, $u_{\text{out}}^{\text{ref}} = 300\,\text{V}$, $d = 0.429$, $L_{1,2,3} = 2 \times 10^{-3}\,\text{H}$, $C = 2 \times 10^{-3}\,\text{F}$, $P_1 = 40\,\text{kW}$, and $P_2 = 2.5\,\text{kW}$.
9) *Bidirectional Buck–boost converter:* $E = 400\,\text{V}$, $u_{\text{out}}^{\text{ref}} = 300\,\text{V}$, $d = 0.429$, $L = 2 \times 10^{-3}\,\text{H}$, $C = 2 \times 10^{-3}\,\text{F}$, $P_1 = 40\,\text{kW}$, and $P_2 = 2.5\,\text{kW}$.

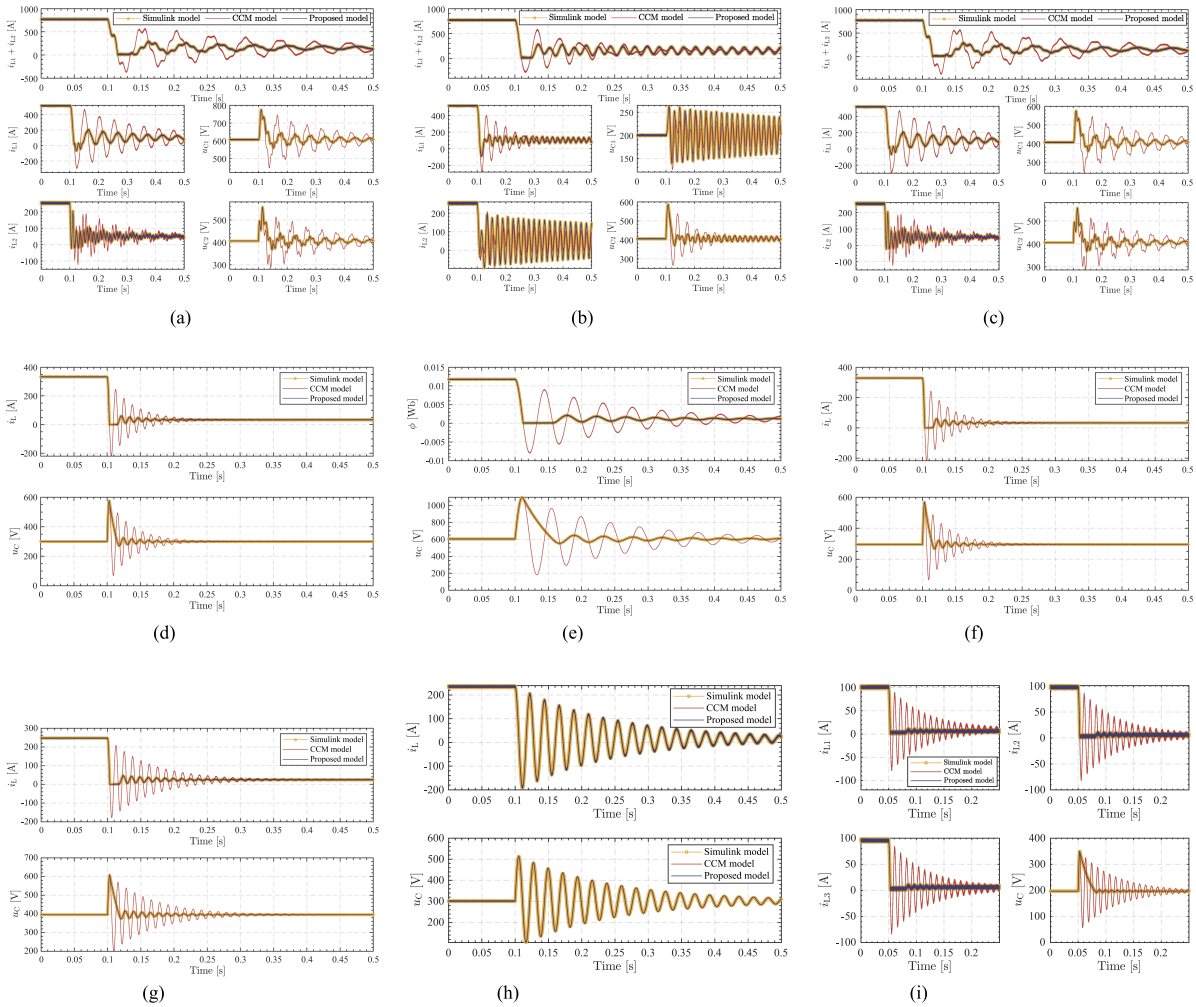

Fig. 20. Outcomes of CCM, simulink, and proposed models. (a) Cuk. (b) Sepic. (c) Zeta. (d) Forward. (e) Flyback. (f) Push–pull. (g) Full-bridge. (h) Bidirectional buck–boost. (i) Multiphase buck–boost.

As illustrated in Fig. 20, the outcomes of the proposed models are in strict accordance with the Simulink results, thereby validating the accuracy of the proposed models in Table I.

REFERENCES

[1] N. Hou, L. Ding, P. Gunawardena, T. Wang, Y. Zhang, and Y. W. Li, "A partial power processing structure embedding renewable energy source and energy storage element for islanded dc microgrid," *IEEE Trans. Power Electron.*, vol. 38, no. 3, pp. 4027–4039, Mar. 2023.

[2] M. S. Khan, S. S. Nag, A. Das, and C. Yoon, "Analysis and control of an input-parallel output-series connected buck-boost DC–DC converter for electric vehicle powertrains," *IEEE Trans. Transport. Electrific.*, vol. 9, no. 2, pp. 2015–2025, Jun. 2023.

[3] M. A. Hassan, C.-L. Su, J. Pou, D. Almakhles, T.-S. Zhan, and K.-Y. Lo, "Robust passivity-based control for interleaved bidirectional DC–DC power converter with constant power loads in DC shipboard microgrid," *IEEE Trans. Transport. Electrific.*, vol. 10, no. 2, pp. 3590–3602, Jun. 2024.

[4] X. Li, W. Jiang, J. Wang, P. Wang, and X. Wu, "An autonomous control scheme of global smooth transitions for bidirectional DC-DC converter in DC microgrid," *IEEE Trans. Energy Convers.*, vol. 36, no. 2, pp. 950–960, Jun. 2021.

[5] Y. Lu and S. Zhong, "Sigmoid function model for a PWM DC–DC converter," *IEEE Trans. Power Electron.*, vol. 38, no. 12, pp. 15327–15337, Dec. 2023.

[6] X. Wei, Y. Lu, and X. Ge, "Sigmoid function model and dynamic characteristics analysis for inductive wireless power transmission control system," *IEEE Trans. Ind. Electron.*, vol. 69, no. 11, pp. 11112–11120, Nov. 2022.

[7] W. He, M. M. Namazi, and J. M. Guerrero, "Adaptive energy-based control for buck converter with a class of nonlinear loads," *IEEE Trans. Circuits Syst. II: Exp. Briefs*, vol. 69, no. 12, pp. 4869–4873, Dec. 2022.

[8] S. Ding, W. X. Zheng, J. Sun, and J. Wang, "Second-order sliding-mode controller design and its implementation for buck converters," *IEEE Trans. Ind. Informat.*, vol. 14, no. 5, pp. 1990–2000, May 2018.

[9] V. Vorperian, "Simplified analysis of PWM converters using model of PWM switch. Continuous conduction mode," *IEEE Trans. Aerosp. Electron. Syst.*, vol. 26, no. 3, pp. 490–496, May 1990.

[10] B. Wang et al., "Event-triggered model predictive control for power converters," *IEEE Trans. Ind. Electron.*, vol. 68, no. 1, pp. 715–720, Jan. 2021.

[11] Z. Karami, Q. Shafiee, S. Sahoo, M. Yaribeygi, H. Bevrani, and T. Dragicevic, "Hybrid model predictive control of DC–DC boost converters with constant power load," *IEEE Trans. Energy Convers.*, vol. 36, no. 2, pp. 1347–1356, Jun. 2021.

[12] R. D. Middlebrook and S. Cuk, "A general unified approach to modelling switching-converter power stages," in *Proc. 1976 IEEE Power Electron. Specialists Conf.*, 1976, pp. 18–34.

[13] E. Van Dijk, J. Spruijt, D. O'Sullivan, and J. Klaassens, "PWM-switch modeling of DC-DC converters," *IEEE Trans. Power Electron.*, vol. 10, no. 6, pp. 659–665, Nov. 1995.

[14] D. Zhan, L. Wei, Y. Zhang, and Y. Yao, "A generalized model of nonisolated multiphase DC–DC converter based on novel switching period averaging method," *IEEE Trans. Power Electron.*, vol. 30, no. 9, pp. 5181–5191, Sep. 2015.

[15] Z. Lin, W. Huang, M. Yu, N. Tai, Y. Zhang, and A. Senkov, "A unified adaptive damping ratio control for multitype DC–DC converters in shipboard power systems," *IEEE Trans. Power Electron.*, vol. 40, no. 4, pp. 5052–5068, Apr. 2025.

[16] Y. Sugimoto, T. Sai, K. Watanabe, and M. Abe, "Feedback loop analysis and optimized compensation slope of the current-mode buck DC-DC converter in DCM," *IEEE Trans. Circuits Syst. I: Reg. Papers*, vol. 62, no. 1, pp. 311–319, Jan. 2015.

[17] Y. Qiu, X. Chen, C. Zhong, and C. Qi, "Uniform models of PWM DC–DC converters for discontinuous conduction mode considering parasitics," *IEEE Trans. Ind. Electron.*, vol. 61, no. 11, pp. 6071–6080, Nov. 2014.

[18] F. L. Tofoli, "Unified small-signal model for DC–DC converters based on the four-state switching cell in discontinuous conduction mode," *IEEE J. Emerg. Sel. Topics Power Electron.*, vol. 12, no. 2, pp. 1946–1958, Apr. 2024.

[19] H.-C. Kim, M. Biswas, and J.-W. Park, "Discontinuous conduction mode analysis of two-phase interleaved buck converter with inversely coupled inductor," *IEEE Access*, vol. 12, pp. 91944–91956, 2024.

[20] Z. Lin, W. Huang, R. Li, N. Tai, and J. Liu, "Adaptive damping ratio control of parallel buck converters for the marine pulsed power loads," *IEEE Trans. Power Electron.*, vol. 39, no. 9, pp. 10989–11006, Sep.– 2024.

[21] X. Wang et al., "Adaptive voltage-guaranteed control of DC/DC-buck-converter-interfaced DC microgrids with constant power loads," *IEEE Trans. Ind. Electron.*, vol. 71, no. 11, pp. 14926–14936, Nov. 2024.

[22] X. Zhang et al., "Adaptive constraints model active mismatch predictive control for power converters of energy storage system," *IEEE Trans. Power Electron.*, vol. 40, no. 9, pp. 13730–13740, Sep. 2025.

[23] Q. Xu, C. Zhang, Z. Xu, P. Lin, and P. Wang, "A composite finite-time controller for decentralized power sharing and stabilization of hybrid fuel cell/supercapacitor system with constant power load," *IEEE Trans. Ind. Electron.*, vol. 68, no. 2, pp. 1388–1400, Feb. 2021.

[24] Y. Chen, B. Zhang, Y. Jiang, F. Xie, D. Qiu, and Y. Chen, "A general frequency-domain model of trailing-edge and leading-edge carrier PWM DC–DC converter based on hybrid continuous and discrete-time descriptions," *IEEE Trans. Emerg. Sel. Topics Power Electron.*, vol. 9, no. 4, pp. 4175–4187, Aug.– 2021.

[25] M. Hejri and H. Mokhtari, "Global hybrid modeling and control of a buck converter: A novel concept," *Int. J. Circuit Theory Appl.*, vol. 37, no. 9, pp. 968–986, 2009.

[26] A. Reindl, F. Lausser, L. Eriksson, S. Park, M. Niemetz, and H. Meier, "Control oriented mathematical modeling of a bidirectional DC-DC converter - Part 1: Buck mode," in *Proc. Int. Conf. Appl. Electron.*, 2023, pp. 1–7.

[27] A. Reindl, F. Lausser, L. Eriksson, S. Park, and M. Niemetz, "Control oriented mathematical modeling of a bidirectional DC-DC converter - Part 2: Boost mode," in *Proc. Int. Conf. Appl. Electron.*, 2023, pp. 1–7.

[28] N. Kumar and A. Agarwal, "Real-time modelling and controlling of boost converter using supervised learning," in *Proc. IEEE 10th Power India Int. Conf.*, 2022, pp. 1–6.

[29] X. Li, F. Lin, J. J. Rodrıǵuez-Andina, J. M. Guerrero, H. A. Mantooth, and H. Ma, "NeurPecs: Physics-informed AI-based adaptive circuit simulator for power converters," *IEEE Trans. Ind. Electron.*, early access, Aug. 8, 2025, doi: 10.1109/TIE.2025.3582591.

[30] O. A. Beg, H. Abbas, T. T. Johnson, and A. Davoudi, "Model validation of PWM DC–DC converters," *IEEE Trans. Ind. Electron.*, vol. 64, no. 9, pp. 7049–7059, Sep. 2017.

[31] M. Hejri, A. Giua, and H. Mokhtari, "On the complexity and dynamical properties of mixed logical dynamical systems via an automaton-based realization of discrete-time hybrid automaton," *Int. J. Robust Nonlinear Control*, vol. 28, no. 16, pp. 4713–4746, 2018.

[32] J. Han, B. Zhang, and D. Qiu, "Bi-switching status modeling method for DC–DC converters in CCM and DCM operations," *IEEE Trans. Power Electron.*, vol. 32, no. 3, pp. 2464–2472, Mar. 2017.

[33] Y. Fang, Y. Chen, B. Zhang, and D. Qiu, "Multimode sequence modeling method for accurate description of VHF resonant converters based on mixed logical inequalities," *IEEE Trans. Power Electron.*, vol. 40, no. 2, pp. 3240–3250, Feb. 2025.